


## Lattice Boltzmann model for capillary interactions between particles at a liquid-vapor interface under gravity

Yasushi Mino <sup>1,\*</sup>, Hazuki Tanaka,<sup>1</sup> Koichi Nakaso,<sup>1</sup> Kuniaki Gotoh <sup>1</sup> and Hiroyuki Shinto <sup>2,†</sup>

<sup>1</sup>*Division of Applied Chemistry, Graduate School of Natural Science and Technology, Okayama University, 3-1-1 Tsushima-naka, Kita-ku, Okayama 700-8530, Japan*

<sup>2</sup>*Department of Chemical Engineering, Fukuoka University, 8-19-1 Nanakuma, Jonan-ku, Fukuoka 814-0180, Japan*



(Received 29 December 2021; accepted 25 March 2022; published 25 April 2022)

A computational technique based on the lattice Boltzmann method (LBM) is developed to simulate the wettable particles adsorbed to a liquid-vapor interface under gravity. The proposed technique combines the improved smoothed-profile LBM for the treatment of moving solid particles in a fluid and the free-energy LBM for the description of a liquid-vapor system. Five benchmark two-dimensional problems are examined: (A) a stationary liquid drop in the vapor phase; a wettable particle adsorbed to a liquid-vapor interface in (B) the absence and (C) the presence of gravity; (D) two freely moving particles at a liquid-vapor interface in the presence of gravity (i.e., capillary flotation forces); and (E) two vertically constrained particles at a liquid-vapor interface (i.e., capillary immersion forces). The simulation results are in good quantitative agreement with theoretical estimations, demonstrating that the proposed technique can reproduce the capillary interactions between wettable particles at a liquid-vapor interface under gravity.

DOI: [10.1103/PhysRevE.105.045316](https://doi.org/10.1103/PhysRevE.105.045316)

### I. INTRODUCTION

Solid particles adsorbed to liquid-fluid (i.e., liquid or gas) interfaces exhibit varied dynamics because of capillary interactions. These generate unique structures via the self-assembly of particles [1–3], and have attracted considerable interest. In industrial fields, the behavior of capillary-interacting particles makes it difficult to control manufacturing processes that treat a solid-liquid-fluid ternary system, such as drying colloidal fluids [4] and particle-stabilized emulsions [5] and foams [6]. To date, the capillary interactions between particles have been extensively investigated both experimentally and theoretically, and theoretical expressions have been derived for the capillary forces acting on two particles in a mechanically equilibrated state [7]. However, it is rather difficult to consider the hydrodynamic effects and the multibody effects on the capillary forces. Thus, numerical simulations are increasingly used as an effective approach for studying multiparticle dynamics in such ternary systems [8,9].

The lattice Boltzmann method (LBM) [10,11] is a good tool for studying complex fluid systems [12]. Although numerical simulations based on the LBM have been used to efficiently simulate the flow dynamics involving movable solid particles or colloids [13–16], it remains challenging to reproduce systems in which solid particles are suspended and/or adsorbed to the liquid-fluid interfaces in multiphase and/or multicomponent fluids. Therefore, various techniques that combine the solid-liquid models with multiphase and/or

multicomponent LBM models have been developed [17–21]. To the best of our knowledge, only a few LB studies [18,21] have presented the force-distance profiles for the capillary forces between movable solid particles at interfaces and compared them with exact theoretical estimations. These models treat two-phase fluids with no density contrast.

In our recent study [22], we proposed a technique that combines the improved smoothed-profile LBM (iSP-LBM) [23] for the treatment of moving solid-fluid boundaries and the free-energy LBM for the description of the dynamics of a binary fluid mixture, where the two immiscible fluids have the same density [24]. Within the framework of the free-energy approach [25,26], the majority of the previous models adopt the wetting boundary condition for solid walls based on Cahn's theory [27,28]. In contrast, we employed an alternative wetting boundary condition [29] for the moving solid particles. In our model, the order parameter distinguishing the two fluids is constrained within the solid domain, and the two-phase flow around the solid object develops naturally to satisfy the wettability conditions of the solid surface. Because of the good compatibility between the iSP method and free-energy LBM, our technique accurately and stably simulates the complex particle dynamics at liquid-liquid interfaces without a substantial increase in computational time. As a result, our simulation results for capillary interactions were generally in good quantitative agreement with the theoretical estimations [22]. As a next step, it is necessary to extend this technique to systems in which the two fluids have different densities, which are observed more generally.

In this study, a one-component, two-phase fluid system, i.e., a liquid-vapor system, involving wettable solid particles is considered. We develop a numerical model that combines the iSP method with the free-energy model proposed by

\*ymino@okayama-u.ac.jp

†hshinto@fukuoka-u.ac.jp

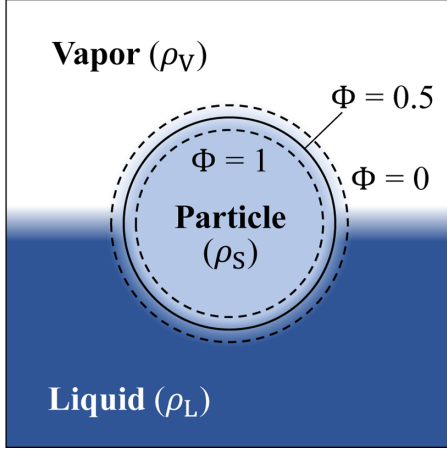


FIG. 1. Schematic illustration of a circular solid particle trapped at the interface between a liquid of density  $\rho_L$  and a vapor of density  $\rho_V$ . The order parameter  $\Phi$  distinguishes the solid particle domain ( $\Phi = 1$ ) from the fluid domain ( $\Phi = 0$ ). The density of the artificial fluid filling the solid particle domain,  $\rho_S$ , is tuned to represent the particle wettability. Note that  $\rho_S$  is generally different from the real mass density of the particles,  $\rho_P$ .

Swift *et al.* [25] for the simulation of capillary interactions between wettable particles at the liquid-vapor interface. To calculate the capillary interactions accurately, it is essential to carefully consider the gravitational and hydrodynamic forces acting on the artificial fluid within the solid particle domain. The proposed model is applied to five benchmark two-dimensional problems: (A) a stationary liquid drop in a vapor phase; a wettable particle adsorbed to a liquid-vapor interface in (B) the absence and (C) the presence of gravity; (D) two freely moving particles at a liquid-vapor interface in the presence of gravity; and (E) two vertically constrained particles at a liquid-vapor interface in the presence of gravity. The results of these simulations are compared with the theoretical estimations.

## II. SIMULATION MODEL

We consider a system in which  $N_p$  solid circular particles are trapped at the interface between a liquid with a density of  $\rho_L$  and a vapor with a density of  $\rho_V$  under gravity, as shown in Fig. 1. The order parameter  $\Phi$  distinguishes the solid particle domain ( $\Phi = 1$ ) from the fluid domain ( $\Phi = 0$ ). In our previous study [22], an additional order parameter was used to represent the two fluids [24], and the constrained value of the order parameter within the particle domain determined the particle wettability. However, in the present model, where the liquid and vapor phases are distinguished by density values [25], the density  $\rho_S$  of the artificial fluid filling the solid particle domain must be tuned to represent the particle wettability. Note that the tuned density of the artificial fluid  $\rho_S$  is generally different from the real mass density of the particles  $\rho_P$ .

### A. Improved smoothed-profile method

In the conventional SP method [16,30], the internal and interfacial domains of solid particles are filled with an artificial fluid. Our previous model assumed that the physical

properties (i.e., density and viscosity) are the same as in the host fluid, which is valid for systems in which particles exist in a mixture of two fluids having the same density and viscosity [22]. However, in the present model, the physical properties of the artificial fluid filling the solid particle domains vary according to the wettability of the particles.

Over the computational domain, including the internal and interfacial domains of solid particles, the hydrodynamics of the fluid [31] is described by the continuity equation and the modified momentum equation:

$$\frac{\partial \rho}{\partial t} + \nabla \cdot (\rho \mathbf{u}) = 0, \quad (1)$$

$$\frac{\partial(\rho \mathbf{u})}{\partial t} + \nabla \cdot (\rho \mathbf{u} \mathbf{u}) = -\nabla \cdot \mathbf{P} + \nabla \cdot \{\eta[\nabla \mathbf{u} + (\nabla \mathbf{u})^T]\} + \rho \mathbf{g} + \rho \Phi \mathbf{f}_P, \quad (2)$$

where  $\rho$  is the fluid density;  $\mathbf{u}$  is the flow velocity;  $\mathbf{P}$  is the modified pressure tensor, through which the thermodynamic properties of the system enter the hydrodynamic description [25];  $\eta$  is the viscosity; and  $\mathbf{g}$  is the gravitational acceleration. The term  $\rho \Phi \mathbf{f}_P$  represents the body force that enforces the no-slip conditions on rigid particle surfaces. In this study, these calculations were conducted within the LBM framework, as described in Sec. II B.

The translational and rotational motions of the  $k$ th circular particle ( $k = 1, 2, \dots, N_p$ ) are described by the Newton-Euler equations:

$$\frac{d\mathbf{X}_k}{dt} = \mathbf{V}_k, \quad (3)$$

$$M_k \frac{d\mathbf{V}_k}{dt} = \mathbf{F}_k^H + \mathbf{F}_k^P + \mathbf{F}_k^G, \quad (4)$$

$$\mathbf{I}_k \cdot \frac{d\boldsymbol{\Omega}_k}{dt} = \mathbf{N}_k^H, \quad (5)$$

where  $\mathbf{X}_k$ ,  $\mathbf{V}_k$ ,  $\boldsymbol{\Omega}_k$ ,  $M_k$ , and  $\mathbf{I}_k$  are the center-of-mass position, translational velocity, rotational velocity, mass, and inertial tensor of the  $k$ th particle, respectively. The terms  $\mathbf{F}_k^H$  and  $\mathbf{N}_k^H$  are the hydrodynamic force and torque, respectively, and  $\mathbf{F}_k^P$  is the force that prevents the particles from overlapping with each other. In the present study,  $\mathbf{F}_k^P$  was represented by the repulsive part of the Lennard-Jones potential for particle-particle and particle-wall direct interactions [30]. The term  $\mathbf{F}_k^G$  represents the gravitational force and must be expressed as  $\mathbf{F}_k^G = M_k(1 - \rho_S/\rho_P)\mathbf{g}$ , which considers the gravitational force acting on the artificial fluid with a density of  $\rho_S$  inside the  $k$ th particle, as described in Sec. II C.

The original sharp interfaces between the solid particles and the host fluid are replaced by diffuse interfaces with a finite thickness of  $\xi_{SP}$ , as shown in Fig. 1. The existence of particles is expressed as a continuous field over the computational domain:

$$\Phi(\mathbf{x}, t) = \sum_{k=1}^{N_p} \Phi_k(\mathbf{x}, t), \quad (6)$$

where  $\Phi_k(\mathbf{x}, t)$  is the smoothed-profile function for the  $k$ th particle at Eulerian lattice node  $\mathbf{x}$  and time  $t$ . This function is defined such that its profile continuously changes from

$\Phi_k = 1$  (particle-side domain) to  $\Phi_k = 0$  (fluid-side domain) within the interfacial domain. In this paper,  $\Phi_k$  is defined as

$$\Phi_k(\mathbf{x}, t) = s(R_k - |\mathbf{x} - \mathbf{X}_k(t)|),$$

$$s(x) = \begin{cases} 0, & x < -\xi_{\text{SP}}/2 \\ \frac{1}{2} \left[ \sin\left(\frac{\pi x}{\xi_{\text{SP}}}\right) + 1 \right], & |x| \leq \xi_{\text{SP}}/2, \\ 1, & x > \xi_{\text{SP}}/2, \end{cases} \quad (7)$$

where  $R_k$  is the radius of the  $k$ th particle.

Using the particle field  $\Phi(\mathbf{x}, t)$ , the particle velocity field  $\mathbf{u}_p(\mathbf{x}, t)$  is defined as

$$\Phi(\mathbf{x}, t) \mathbf{u}_p(\mathbf{x}, t) = \sum_{k=1}^{N_p} \Phi_k(\mathbf{x}, t) [\mathbf{V}_k(t) + \boldsymbol{\Omega}_k(t) \times (\mathbf{x} - \mathbf{X}_k(t))]. \quad (8)$$

The total (fluid + particle) velocity field  $\mathbf{u}(\mathbf{x}, t)$  is then expressed as

$$\mathbf{u}(\mathbf{x}, t) = (1 - \Phi) \mathbf{u}_F + \Phi \mathbf{u}_p = \mathbf{u}_F + \Phi(\mathbf{u}_p - \mathbf{u}_F). \quad (9)$$

To derive the evolution of the total velocity  $\mathbf{u}$ , we solve for the fluid velocity  $\mathbf{u}_F$  [30]. The total velocity is predicted to be  $\mathbf{u}^* = \mathbf{u}_F$  without the body force term  $\rho \Phi \mathbf{f}_p$ . To enforce Eq. (9) and the solid-fluid impermeability condition, the time-integrated body force is calculated as

$$\int_t^{t+\Delta t} \rho \Phi \mathbf{f}_p dt' = \rho \Phi(\mathbf{x}, t + \Delta t) [\mathbf{u}_p(\mathbf{x}, t + \Delta t) - \mathbf{u}^*(\mathbf{x}, t + \Delta t)]. \quad (10)$$

Correcting  $\mathbf{u}^*$  with the body force gives the total velocity field  $\mathbf{u}(\mathbf{x}, t + \Delta t)$ .

In the iSP method [23], the hydrodynamic force  $\mathbf{F}_k^H$  and torque  $\mathbf{N}_k^H$  acting on the  $k$ th particle at time  $t$  are calculated based on the momentum exchange between the particle and host fluid during the time interval  $\Delta t$ :

$$\mathbf{F}_k^H(t) = \mathbf{F}_k^{\text{H,tot}}(t) + \mathbf{F}_k^{\text{H,in}}(t), \quad (11)$$

$$\mathbf{N}_k^H(t) = \mathbf{N}_k^{\text{H,tot}}(t) + \mathbf{N}_k^{\text{H,in}}(t), \quad (12)$$

where  $\mathbf{F}_k^{\text{H,tot}}$  and  $\mathbf{N}_k^{\text{H,tot}}$  are the hydrodynamic force and torque calculated using the volume integral of the body force over the  $k$ th particle volume [30]:

$$\mathbf{F}_k^{\text{H,tot}}(t) = - \int_{\Omega^k(t)} \rho \Phi_k \mathbf{f}_p(\mathbf{x}, t) d\mathbf{x}, \quad (13)$$

$$\mathbf{N}_k^{\text{H,tot}}(t) = - \int_{\Omega^k(t)} [\mathbf{x} - \mathbf{X}_k(t)] \times \rho \Phi_k \mathbf{f}_p(\mathbf{x}, t) d\mathbf{x}, \quad (14)$$

in which  $\Omega^k(t)$  represents the domain for the  $k$ th particle with  $\Phi_k(\mathbf{x}, t) > 0$  at time  $t$ . Note that  $\mathbf{F}_k^{\text{H,tot}}$  and  $\mathbf{N}_k^{\text{H,tot}}$  contain the force and torque that compel the velocity of the artificial fluid inside the  $k$ th particle to be consistent with the translational and rotational velocities of the particle, respectively. Therefore, for calculations of the actual hydrodynamic force  $\mathbf{F}_k^H$  and torque  $\mathbf{N}_k^H$ ,  $\mathbf{F}_k^{\text{H,tot}}$  and  $\mathbf{N}_k^{\text{H,tot}}$  must be compensated with the force and torque that compel the velocity of the artificial fluid inside the particle, respectively. This compensation force

$\mathbf{F}_k^{\text{H,in}}$  and torque  $\mathbf{N}_k^{\text{H,in}}$  can be calculated simply using the time derivatives of the linear and angular momenta:

$$\mathbf{F}_k^{\text{H,in}}(t) = \frac{\rho_S}{\rho_P} M_k \frac{d\mathbf{V}_k(t)}{dt}, \quad (15)$$

$$\mathbf{N}_k^{\text{H,in}}(t) = \frac{\rho_S}{\rho_P} \mathbf{I}_k \cdot \frac{d\boldsymbol{\Omega}_k(t)}{dt}. \quad (16)$$

By considering the effect of the internal fluid mass, the iSP method calculates the hydrodynamic force and torque more precisely, resulting in stable and accurate computations of the particle motions in various scenarios. A detailed description of the iSP method can be found in Ref. [23].

One famous method conceptually similar to the SP method is the fluid particle dynamics (FPD) method [32], which mimics the solid particle by a liquid droplet with a very high viscosity. This treatment for the solid particle is not so compatible with the LBM, because the LBM basically requires special techniques for stable calculations of two-phase fluids with a large viscosity contrast. Consequently, we have used the SP method for the treatment of moving solid particles within the LBM framework.

## B. Free-energy lattice Boltzmann method

To simulate liquid-vapor two-phase flows, the free-energy LBM proposed by Swift *et al.* [25] is employed, with a correction to ensure Galilean invariance [33]. Hereafter, we use the dimensionless variables that are defined based on the characteristic length  $L_0$ , flow speed  $U_0$ , imaginary particle speed  $c$ , timescale  $t_0 (=L_0/U_0)$ , and reference density  $\rho_0$ .

We describe the bulk properties of the fluids far away from solid particles through a Landau free-energy functional:

$$F = \int [f_0(\rho, T) + \frac{\kappa}{2} |\nabla \rho|^2] d\mathbf{x}, \quad (17)$$

where  $f_0(\rho, T)$  is the bulk free-energy density and  $T$  is the temperature. The second term gives the excess free-energy density stored at the liquid-vapor interface, and  $\kappa$  is a constant related to the interfacial tension.

The bulk free-energy density can be conveniently expressed as [27,31]

$$f_0(\rho, T) = p_c(\nu_\rho + 1)^2(\nu_\rho^2 - 2\nu_\rho + 3 - 2\beta\tau_w), \quad (18)$$

where  $\nu_\rho = (\rho - \rho_c)/\rho_c$ ;  $\tau_w = (T_c - T)/T_c$ ; and  $p_c$ ,  $\rho_c$ , and  $T_c$  are the critical pressure, density, and temperature, respectively.  $\beta$  is a constant that can be tuned to control the liquid-vapor density ratio. For  $T < T_c$ , there are two coexisting phases with densities of  $\rho_L = \rho_c(1 + \sqrt{\beta\tau_w})$  and  $\rho_V = \rho_c(1 - \sqrt{\beta\tau_w})$ . Equation (18) provides the following liquid-vapor interface profile:

$$\rho^{\text{int}} = \rho_c \left[ 1 + \sqrt{\beta\tau_w} \tanh\left(\frac{x'}{\sqrt{2}\xi_{\text{LV}}}\right) \right], \quad (19)$$

where  $x'$  is the coordinate normal to the interface, which is positioned at  $x' = 0$ , and  $\xi_{\text{LV}}$  is the width of the liquid-vapor interface, defined as

$$\xi_{\text{LV}} = \sqrt{\frac{\kappa \rho_c^2}{4\beta\tau_w p_c}}. \quad (20)$$

The interfacial tension  $\sigma_{LV}$  is obtained by

$$\begin{aligned}\sigma_{LV} &= \kappa \int_{-\infty}^{\infty} \left( \frac{\partial \rho_{\text{int}}}{\partial x'} \right)^2 dx' \\ &= \sqrt{2\kappa p_c (\beta \tau_w)^{3/2}} \rho_c \int_{-1}^1 (1 - \chi_{\text{int}}^2) d\chi_{\text{int}} \\ &= \frac{4}{3} \sqrt{2\kappa p_c (\beta \tau_w)^{3/2}} \rho_c,\end{aligned}\quad (21)$$

where  $\chi_{\text{int}} \equiv (\rho_{\text{int}} - \rho_c) / (\rho_L - \rho_c)$ .

The pressure tensor for a liquid-vapor system is given by

$$P_{\alpha\beta} = \left( p_0 - \kappa \rho \nabla^2 \rho - \frac{\kappa}{2} |\nabla \rho|^2 \right) \delta_{\alpha\beta} + \kappa \frac{\partial \rho}{\partial x_\alpha} \frac{\partial \rho}{\partial x_\beta}, \quad (22)$$

$$p_0 = \rho \frac{\partial f_0}{\partial \rho} - f_0 = p_c (v_\rho + 1)^2 (3v_\rho^2 - 2v_\rho + 1 - 2\beta \tau_w), \quad (23)$$

where the subscripts  $\alpha$  and  $\beta$  represent the Cartesian coordinates ( $\alpha, \beta = x, y$ ), and the summation convention is applied to  $\alpha$  and  $\beta$ . Equation (23) is the equation of state of the fluid, and  $p_0$  can be interpreted as the bulk pressure far from the interface, where the gradient terms are zero.

In this study, the two-dimensional nine-velocity (D2Q9) model is used. The physical space of interest is divided into a square lattice, and the fluid flow is represented by a collection of imaginary fluid particles with nine velocity vectors  $\mathbf{c}_i$  [= (0, 0), ( $\pm 1, 0$ ), (0,  $\pm 1$ ), and ( $\pm 1, \pm 1$ ) for  $i = 1, 2, \dots, 9$ ]. The particle distribution function  $f_i(\mathbf{x}, t)$  with velocity  $\mathbf{c}_i$  at lattice site  $\mathbf{x}$  and time  $t$  evolves as follows:

$$\begin{aligned}f_i(\mathbf{x} + \mathbf{c}_i \Delta x, t + \Delta t) &= f_i(\mathbf{x}, t) - \frac{1}{\tau} [f_i(\mathbf{x}, t) - f_i^{\text{eq}}(\mathbf{x}, t)], \\ &\text{for } i = 1, 2, \dots, 9,\end{aligned}\quad (24)$$

where  $f_i^{\text{eq}}$  is the local equilibrium distribution function,  $\tau$  is the dimensionless single relaxation time,  $\Delta x$  is the spacing of the square lattice, and  $\Delta t$  is the time step during which the particles travel across the lattice spacing. Note that  $\Delta t = \text{Sh} \Delta x$ , where Sh denotes the Strouhal number,  $\text{Sh} = L_0 / (t_0 c) = U_0 / c$ . The physical variables are related to the distribution functions by

$$\rho(\mathbf{x}, t) = \sum_{i=1}^9 f_i(\mathbf{x}, t), \quad (25)$$

$$\mathbf{u}(\mathbf{x}, t) = \frac{1}{\rho(\mathbf{x}, t)} \sum_{i=1}^9 \mathbf{c}_i f_i(\mathbf{x}, t). \quad (26)$$

The equilibrium distribution function is written as [33]

$$\begin{aligned}f_i^{\text{eq}}(\mathbf{x}, t) &= H_i \rho + F_i \left[ (p_0 - \kappa \rho \nabla^2 \rho) + 2\omega u_\gamma \frac{\partial \rho}{\partial x_\gamma} \right] \\ &\quad + E_i \rho \left[ 3u_\alpha c_{i\alpha} - \frac{3}{2} u^2 + \frac{9}{2} u_\alpha u_\beta c_{i\alpha} c_{i\beta} \right] \\ &\quad + E_i G_{\alpha\beta} c_{i\alpha} c_{i\beta},\end{aligned}\quad (27)$$

with

$$\begin{aligned}H_1 &= 1, \quad H_{2-9} = 0, \\ F_1 &= -5/3, \quad F_{2-5} = 1/3, \quad F_{6-9} = 1/12, \\ E_1 &= 4/9, \quad E_{2-5} = 1/9, \quad E_{6-9} = 1/36,\end{aligned}\quad (28)$$

and

$$\begin{aligned}G_{\alpha\beta} &= \frac{9}{2} \left[ \kappa \frac{\partial \rho}{\partial x_\alpha} \frac{\partial \rho}{\partial x_\beta} + \omega \left( u_\beta \frac{\partial \rho}{\partial x_\alpha} + u_\alpha \frac{\partial \rho}{\partial x_\beta} \right) \right] \\ &\quad - \frac{9}{4} \left[ \kappa \frac{\partial \rho}{\partial x_\gamma} \frac{\partial \rho}{\partial x_\gamma} + 2\omega u_\gamma \frac{\partial \rho}{\partial x_\gamma} \right] \delta_{\alpha\beta},\end{aligned}\quad (29)$$

where the parameter  $\omega$  is needed to recover Galilean invariance, the subscript  $\gamma$  represents the Cartesian coordinates ( $\gamma = x, y$ ),  $\delta_{\alpha\beta}$  is the Kronecker delta, and the summation convention is applied to  $\alpha, \beta$ , and  $\gamma$ .

The derivatives in Eqs. (27) and (29) are computed using the finite difference schemes,

$$\frac{\partial \rho}{\partial x_\alpha} \approx \frac{3}{\Delta x} \sum_{i=2}^9 E_i c_{i\alpha} \rho(\mathbf{x} + \mathbf{c}_i \Delta x), \quad (30)$$

$$\nabla^2 \rho \approx \frac{6}{(\Delta x)^2} \sum_{i=2}^9 E_i [\rho(\mathbf{x} + \mathbf{c}_i \Delta x) - \rho(\mathbf{x})], \quad (31)$$

which improve the stencil isotropy of the numerical derivatives, resulting in a reduction in spurious velocities [34].

The relaxation parameter  $\tau$  is related to the dimensionless kinematic viscosity according to

$$v = \frac{1}{3} \left( \tau - \frac{1}{2} \right) \Delta x, \quad (32)$$

and the parameter needed to recover Galilean invariance [33] is given by

$$\omega = \frac{1}{3} \left( \tau - \frac{1}{2} \right) \Delta x. \quad (33)$$

In the presence of an external body force  $\mathbf{f}(\mathbf{x}, t)$ , the evolution of the particle distribution function  $f_i(\mathbf{x}, t)$  [Eq. (24)] is calculated by a fractional step approach. The intermediate value of  $f_i$  without the body force, denoted by  $f_i^*$ , is calculated as

$$f_i^*(\mathbf{x} + \mathbf{c}_i \Delta x, t + \Delta t) = f_i(\mathbf{x}, t) - \frac{1}{\tau} [f_i(\mathbf{x}, t) - f_i^{\text{eq}}(\mathbf{x}, t)]. \quad (34)$$

Then,  $f_i$  is obtained by correcting  $f_i^*$  with the body force as

$$f_i(\mathbf{x}, t + \Delta t) = f_i^*(\mathbf{x}, t + \Delta t) + 3\Delta x E_i \mathbf{c}_i \cdot \mathbf{f}(\mathbf{x}, t + \Delta t). \quad (35)$$

### C. Coupling between the iSP method and free-energy LBM

To couple the iSP method with the free-energy LBM, the wettability of the solid particle surface is represented using the method of Ref. [22], in which the compositional order parameter for the immiscible two-phase fluid is constrained at the particle domain defined in the SP algorithm to represent the wettability of a particle surface. In the present model, because one component is treated without the compositional order parameter, the density of the artificial fluid at the particle domain must be constrained to  $\rho_S$  ( $\rho_S \leq \rho \leq \rho_L$ ) (Fig. 1). The free-energy functional of Eq. (17) is thus replaced by

$$F = \int \left[ f_0(\rho, T) + \frac{\kappa}{2} |\nabla \rho|^2 + \frac{\kappa_S}{2} \Phi'(\rho - \rho_S)^2 \right] dx, \quad (36)$$

where the additional third term in the integral contains a positive parameter  $\kappa_S$  and the modified particle field function  $\Phi'(\mathbf{x}, t)$  to represent the wettability of a particle surface. Instead of using Eqs. (6) and (7), the field  $\Phi'(\mathbf{x}, t)$  is calculated as follows:

$$\Phi'(\mathbf{x}, t) = \sum_{k=1}^{N_p} \Phi'_k(\mathbf{x}, t), \quad (37)$$

$$\Phi'_k(\mathbf{x}, t) = s[R_k - |\mathbf{x} - \mathbf{X}_k(t)| - \xi_{SP}/2], \quad (38)$$

where  $s(x)$  is identical to that in Eq. (7). Note that  $\kappa_S$  must be sufficiently large for the free-energy density inside the particles ( $\Phi' = 1$ ) without an interface,  $f_0(\rho, T) + \frac{\kappa_S}{2}(\rho - \rho_S)^2$ , to exhibit a single-well profile with a minimum at  $\rho \approx \rho_S$ .

In the presence of particles, the pressure tensor  $P_{\alpha\beta}$  [Eq. (22)] must be replaced by

$$P_{\alpha\beta} = \left( p_0^S - \kappa \rho \nabla^2 \rho - \frac{\kappa}{2} |\nabla \rho|^2 \right) \delta_{\alpha\beta} + \kappa \frac{\partial \rho}{\partial x_\alpha} \frac{\partial \rho}{\partial x_\beta}, \quad (39)$$

$$p_0^S = \rho \frac{\partial}{\partial \rho} \left[ f_0 + \frac{\kappa_S}{2} \Phi'(\rho - \rho_S)^2 \right] - \left[ f_0 + \frac{\kappa_S}{2} \Phi'(\rho - \rho_S)^2 \right] = p_0 + \frac{\kappa_S}{2} \Phi'(\rho^2 - \rho_S^2). \quad (40)$$

The equilibrium distribution function in Eq. (27) is then calculated with  $p_0^S$  instead of  $p_0$ . When the above modification is introduced, the fluid density exhibits a value of  $\rho \approx \rho_S$  within the particle domain and seamlessly changes to the original value of  $\rho$  for the host fluid outside the particle domain (i.e.,  $\rho_L$  or  $\rho_V$ ). Consequently, the motion of contact points (in the two-dimensional system), where the three phases of the solid particles and liquid and vapor meet, is represented thermodynamically.

The interfacial tensions between the solid surface and the liquid and vapor,  $\sigma_{SL}$  and  $\sigma_{SV}$ , respectively, can be obtained in the same manner as  $\sigma_{LV}$  [Eq. (21)]:

$$\sigma_{SL} = \frac{\sqrt{2\kappa p_c} (\beta \tau_w)^{3/2} \rho_c}{3} (2 - 3\chi_S + \chi_S^3), \quad (41)$$

$$\sigma_{SV} = \frac{\sqrt{2\kappa p_c} (\beta \tau_w)^{3/2} \rho_c}{3} (2 + 3\chi_S - \chi_S^3), \quad (42)$$

where  $\chi_S \equiv (\rho_S - \rho_c)/(\rho_L - \rho_c)$  represents the affinity of the solid surface for the fluids; as  $\chi_S$  approaches 1, the surface affinity for the liquid increases, while as  $\chi_S$  approaches  $-1$ , the surface affinity for vapor increases. The equilibrium contact angle of a solid surface against liquid in the vapor phase,  $\alpha^{\text{th}}$ , is theoretically calculated by Young's law:

$$\cos \alpha^{\text{th}} = \frac{\sigma_{SV} - \sigma_{SL}}{\sigma_{LV}} = \frac{\chi_S}{2} (3 - \chi_S^2). \quad (43)$$

Finally, note the gravitational force term in Eq. (4). In our previous model [22], the gravitational force acting on the fluid was neglected, which is acceptable for isodense two-phase fluid systems. However, when treating a two-phase fluid with a density contrast under gravity, the gravitational force acting on the fluid cannot generally be neglected. Such a situation requires special care of the gravitational force acting on the

artificial fluid at the particle domain as well as the host fluid. In the iSP algorithm, the gravitational force acting on the artificial fluid of density  $\rho_S$  inside the  $k$ th particle,  $M_k(\rho_S/\rho_P)\mathbf{g}$ , is naturally included in the exact hydrodynamic force acting on the  $k$ th particle,  $\mathbf{F}_k^H(t)$ , and must be compensated in Newton's equation, as described in Eq. (4). Without this treatment, movable particles exhibit unphysical behavior, leading to unstable calculations.

#### D. Computational procedure

At the initial step ( $t = 0$ ),  $\mathbf{X}_k(0)$ ,  $\mathbf{V}_k(0)$ ,  $\boldsymbol{\Omega}_k(0)$ ,  $\Phi(\mathbf{x}, 0)$ ,  $\rho(\mathbf{x}, 0)$ , and  $\mathbf{u}(\mathbf{x}, 0)$  are assigned, and  $f_i(\mathbf{x}, 0)$  is assumed to be  $f_i^{\text{eq}}(\mathbf{x}, 0)$ , while  $\mathbf{F}_k^H(t)$  and  $\mathbf{N}_k^H(t)$  are assumed to be zero. It is also assumed that  $\mathbf{X}_k(t)$ ,  $\mathbf{V}_k(t)$ ,  $\boldsymbol{\Omega}_k(t)$ ,  $\Phi(\mathbf{x}, t)$ ,  $\rho(\mathbf{x}, t)$ ,  $\mathbf{u}(\mathbf{x}, t)$ , and  $f_i(\mathbf{x}, t)$  are known immediately prior to being updated at time  $t + \Delta t$ . The computational procedure is described below.

*Step 1.* With the forces and torques at time  $t$ ,  $\mathbf{V}_k(t + \Delta t)$  and  $\boldsymbol{\Omega}_k(t + \Delta t)$  are calculated using Eqs. (4) and (5) through a first-order explicit Euler scheme:

$$\mathbf{V}_k(t + \Delta t) = \mathbf{V}_k(t) + \frac{\Delta t}{\text{Sh}} M_k^{-1} [\mathbf{F}_k^H(t) + \mathbf{F}_k^P(t) + \mathbf{F}_k^G(t)], \quad (44)$$

$$\boldsymbol{\Omega}_k(t + \Delta t) = \boldsymbol{\Omega}_k(t) + \frac{\Delta t}{\text{Sh}} \mathbf{I}_k^{-1} \cdot \mathbf{N}_k^H(t). \quad (45)$$

The center-of-mass position  $\mathbf{X}_k(t + \Delta t)$  is updated using Eq. (3) using a Crank-Nicolson scheme:

$$\mathbf{X}_k(t + \Delta t) = \mathbf{X}_k(t) + \frac{\Delta t}{2\text{Sh}} [\mathbf{V}_k(t) + \mathbf{V}_k(t + \Delta t)]. \quad (46)$$

*Step 2.* Fields  $\Phi(t + \Delta t)$  and  $\mathbf{u}_p(t + \Delta t)$  are calculated using Eqs. (6)–(8) with  $\mathbf{X}_k(t + \Delta t)$ ,  $\mathbf{V}_k(t + \Delta t)$ , and  $\boldsymbol{\Omega}_k(t + \Delta t)$ .

*Step 3a.*  $f_i^*(\mathbf{x}, t + \Delta t)$  is calculated using Eq. (34) and Eqs. (27)–(29) with  $p_0^S$  calculated using Eq. (40), and then the intermediate values  $\rho^*(\mathbf{x}, t + \Delta t)$  and  $\mathbf{u}^*(\mathbf{x}, t + \Delta t)$  are calculated using Eqs. (25) and (26):

$$\rho^*(\mathbf{x}, t + \Delta t) = \sum_{i=1}^9 f_i^*(\mathbf{x}, t + \Delta t), \quad (47)$$

$$\mathbf{u}^*(\mathbf{x}, t + \Delta t) = \frac{1}{\rho^*} \sum_{i=1}^9 \mathbf{c}_i f_i^*(\mathbf{x}, t + \Delta t). \quad (48)$$

The body force  $\rho^* \Phi \mathbf{f}_p(\mathbf{x}, t + \Delta t)$  is calculated using Eq. (10):

$$\rho^* \Phi \mathbf{f}_p(\mathbf{x}, t + \Delta t) = \rho^* \Phi(\mathbf{x}, t + \Delta t) \frac{\text{Sh}}{\Delta t} [\mathbf{u}_p(\mathbf{x}, t + \Delta t) - \mathbf{u}^*(\mathbf{x}, t + \Delta t)]. \quad (49)$$

*Step 3b.*  $f_i(\mathbf{x}, t + \Delta t)$  is calculated using Eq. (35) as follows:

$$f_i(\mathbf{x}, t + \Delta t) = f_i^*(\mathbf{x}, t + \Delta t) + 3\Delta x E_i \mathbf{c}_i \cdot \rho^* \Phi \mathbf{f}_p(\mathbf{x}, t + \Delta t). \quad (50)$$

Then,  $\rho(\mathbf{x}, t + \Delta t)$  and  $\mathbf{u}(\mathbf{x}, t + \Delta t)$  are calculated using Eqs. (25) and (26), respectively.

TABLE I. Parameters of simulated systems.

System	$N_p$	$R/\Delta x$	$\alpha_1$	$\alpha_2$	$\rho_{p1}^* (= \frac{\rho_{p1} - \rho_c}{\rho_L - \rho_c})$	$\rho_{p2}^*$	$L/\Delta x$	$(q\Delta x)^{-1}$	Bo	$(L_x/\Delta x) \times (L_y/\Delta x)$
A	0									$120 \times 120^a$
B	1	5–20	$15^\circ$ – $165^\circ$		2.0					$200 \times 100^b$
C	1	10	$45^\circ, 90^\circ, 135^\circ$		–2.0–5.3			14.1	0.50	$400 \times 100^c$
D.1	2	10	$45^\circ, 90^\circ, 135^\circ$	$=\alpha_1$	2.0	2.0	24–80	14.1	0.50	$400 \times 100^d$
D.2	2	10	$45^\circ, 90^\circ, 135^\circ$	$=\alpha_1$	–2.0	–2.0	24–80	14.1	0.50	$400 \times 100^d$
D.3	2	10	$135^\circ$	$45^\circ$	2.0	–2.0	24–80	14.1	0.50	$400 \times 100^d$
D.4	2	10	$90^\circ$	$=\alpha_1$	2.0, 5.0	$=\rho_{p1}^*$	40	14.1	0.50	$400 \times 100^d$
E	2	10	$45^\circ, 90^\circ, 135^\circ$	$=\alpha_1$	2.0	2.0	40	14.1	0.50	$400 \times 100^e$

<sup>a</sup>A circular drop of liquid with a radius of  $R_d = (10\text{--}50)\Delta x$  was placed at the center of a simulation cell represented by the  $120 \times 120$  lattice nodes at  $\mathbf{x} = (k\Delta x, l\Delta x)$  for  $k, l = 1, 2, \dots, 120$  (i.e.,  $L_x = L_y = 120\Delta x$ ), and the other region was filled with a host fluid in the vapor phase. The periodic boundary condition was applied in all directions at  $x = \Delta x$  and  $L_x$  and  $y = \Delta x$  and  $L_y$ .

<sup>b</sup>The region containing the fluid and single particle was represented by the  $200 \times 100$  lattice nodes at  $\mathbf{x} = (k\Delta x, l\Delta x)$  for  $k = 1, 2, \dots, 200$  and  $l = 1, 2, \dots, 100$  (i.e.,  $L_x = 200\Delta x$  and  $L_y = 100\Delta x$ ). The lower and upper halves of the simulation cell outside the particle domain were filled with liquid and vapor, respectively. The lower substrate at  $y = 0$  had a density of  $\rho_L$  ( $\chi_S = 1$ ), while the upper substrate at  $y = L_y + \Delta x$  had a density of  $\rho_V$  ( $\chi_S = -1$ ). The halfway free-slip boundary condition was imposed on the fluid-side nodes at  $y = \Delta x$  and  $L_y$  next to the solid-side nodes. The periodic boundary condition was applied on the sides at  $x = \Delta x$  and  $L_x$ .

<sup>c</sup>Same as footnote b, but with  $L_x = 400\Delta x$ .

<sup>d</sup>Same as footnote c, but for a two-particle system.

<sup>e</sup>Same as footnote d, but the area fraction of the liquid phase ranged from 0.4 to 0.6.

Step 4.  $\mathbf{F}_k^{\text{H,tot}}(t + \Delta t)$  and  $N_k^{\text{H,tot}}(t + \Delta t)$  are calculated using Eqs. (13) and (14), respectively, with Eq. (49) as follows:

$$\mathbf{F}_k^{\text{H,tot}}(t + \Delta t) = -\frac{\text{Sh}}{\Delta t} \sum_{\mathbf{x} \in \Omega_{\text{all}}} \rho^* \Phi_k \mathbf{f}_p(\mathbf{x}, t + \Delta t) (\Delta x)^2, \quad (51)$$

$$N_k^{\text{H,tot}}(t + \Delta t) = -\frac{\text{Sh}}{\Delta t} \sum_{\mathbf{x} \in \Omega_{\text{all}}} [\mathbf{x} - \mathbf{X}_k(t + \Delta t)] \times \rho^* \Phi_k \mathbf{f}_p(\mathbf{x}, t + \Delta t) (\Delta x)^2, \quad (52)$$

where  $\Omega_{\text{all}}$  is the entire domain of the system.  $\mathbf{F}_k^{\text{H,in}}(t + \Delta t)$  and  $N_k^{\text{H,in}}(t + \Delta t)$  are calculated using Eqs. (15) and (16) as

$$\mathbf{F}_k^{\text{H,in}}(t + \Delta t) = \frac{\rho_S}{\rho_P} M_k \text{Sh} \frac{\mathbf{V}_k(t + \Delta t) - \mathbf{V}_k(t)}{\Delta t}, \quad (53)$$

$$N_k^{\text{H,in}}(t + \Delta t) = \frac{\rho_S}{\rho_P} \mathbf{I}_k \cdot \text{Sh} \frac{\boldsymbol{\Omega}_k(t + \Delta t) - \boldsymbol{\Omega}_k(t)}{\Delta t}, \quad (54)$$

respectively. Finally,  $\mathbf{F}_k^{\text{H}}(t + \Delta t)$  and  $N_k^{\text{H}}(t + \Delta t)$  are calculated using Eqs. (11) and (12), respectively.

### III. RESULTS AND DISCUSSION

To test the performance of the proposed model, we considered five benchmark problems: (A) a stationary liquid drop in a vapor phase; a wettable particle adsorbed to a liquid-vapor interface in (B) the absence and (C) the presence of gravity; (D) two freely moving particles at a liquid-vapor interface in the presence of gravity (i.e., capillary flotation forces); and (E) two vertically constrained particles at a liquid-vapor interface in the presence of gravity (i.e., capillary immersion forces). Systems C–E, which consider nonzero gravity [ $\mathbf{g} = (0, -g)$ ],

can be characterized by the Bond number Bo and the capillary length  $q^{-1}$ , which are defined as [35,36]:

$$\text{Bo} = q^2 R^2, \quad (55)$$

$$q^{-1} = \sqrt{\frac{\sigma_{\text{LV}}}{(\rho_L - \rho_V)g}}. \quad (56)$$

For  $\text{Bo} \ll 1$ , the capillary forces are dominant, while for  $\text{Bo} \gg 1$ , gravity is the dominant force. The results obtained from the LB simulations were compared with the theoretical estimations. The theoretical descriptions for systems C–E are provided in the Appendix.

The details of the five systems are summarized in Table I, where  $N_p$  is the number of particles,  $R$  is the radius of a particle,  $\alpha$  is the equilibrium contact angle of a particle against liquid in vapor, and  $\rho_p^*$  is the relative particle density, defined as

$$\rho_p^* = \frac{\rho_p - \rho_c}{\rho_L - \rho_c}. \quad (57)$$

The size of the simulation cell  $L_x \times L_y$  for system A was set such that the periodic boundary conditions hardly affected the behavior of a stationary drop. For systems B–E, the horizontal length  $L_x$  was set to be much larger than the capillary length, and the vertical length  $L_y$  was set such that the boundary conditions at the lower and upper walls barely influenced the behavior of the particle(s) at the mechanically equilibrated state.

The following parameters were fixed throughout the present calculations, although it is possible to improve the calculation accuracy by tuning the parameters according to each benchmark problem. Constant values of  $\Delta x$  and  $\Delta t$  were used, giving a constant Strouhal number  $\text{Sh} (= \Delta t / \Delta x)$ . The thickness for the SP function of Eq. (7) was set to  $\xi_{\text{SP}} = 2\Delta x$  to guarantee satisfactory accuracy in reproducing the hydrodynamic force acting on a particle [23]. The parameters

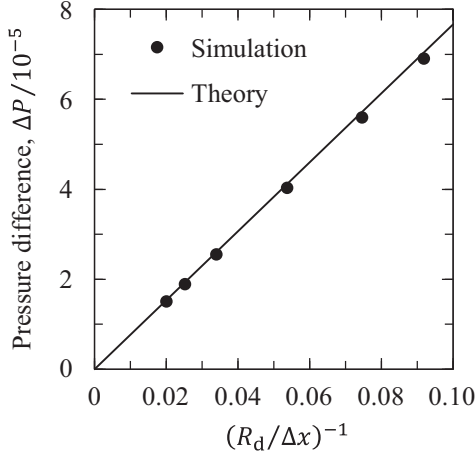


FIG. 2. Pressure difference  $\Delta P$  between the internal and external regions of a circular liquid drop as a function of its inverse radius  $R_d^{-1}$  for system A (see Table I). The filled circles represent the simulation results, and the solid line represents the theoretical estimations based on Laplace's law [Eq. (58)] with interfacial tension of  $\sigma_{LV} = (7.67 \times 10^{-4})\Delta x$ .

determining the bulk free-energy density of Eq. (18) were set to  $\beta\tau_w = 0.03$ ,  $\kappa = 0.004(\Delta x)^2$ ,  $p_c = 0.125$ , and  $\rho_c = 3.5$  [31], resulting in liquid and vapor densities of  $\rho_L = 4.11$  and  $\rho_V = 2.89$ , respectively, and giving an interfacial tension at the liquid-vapor interface of  $\sigma_{LV} = (7.67 \times 10^{-4})\Delta x$  and the interfacial width of  $\xi_{LV} = 1.81\Delta x$ . The effective thickness of the interfacial profile expressed by Eq. (19) should be considered as  $4.164\xi_{LV} (=7.54\Delta x)$  according to Ref. [37]. The relaxation time for  $f_i$  in Eq. (34) was set to  $\tau = 0.8$ . The parameter constraining the density of the artificial fluid at the particle domain to be  $\rho_S$  through the free-energy functional of Eq. (36) was set to  $\kappa_S = 0.01$ .

### A. Single stationary liquid drop in the vapor phase

Let us consider system A in Table I, where a circular liquid drop with a radius of  $R_d$  in vapor was simulated. Figure 2 shows the pressure difference  $\Delta P$  between the internal and external regions of the drop as a function of  $R_d^{-1}$ . The simulation results are in good quantitative agreement with the theoretical estimation based on Laplace's law with the interfacial tension given by Eq. (21),  $\sigma_{LV} = (7.67 \times 10^{-4})\Delta x$ :

$$\Delta P^{\text{th}} = \frac{\sigma_{LV}}{R_d}. \quad (58)$$

This result demonstrates that the present two-phase LBM solver with the above parameters can accurately represent a liquid-vapor interface.

### B. Single particle adsorbed to the liquid-vapor interface in the absence of gravity

System B in Table I was used to investigate the wettability of a particle surface for a liquid-vapor fluid. A particle adsorbed to the liquid-vapor interface was simulated in the absence of gravity. A circular particle of radius  $R$ , mass density  $\rho_P$ , and wettability  $\chi_S$  was initially placed at the center

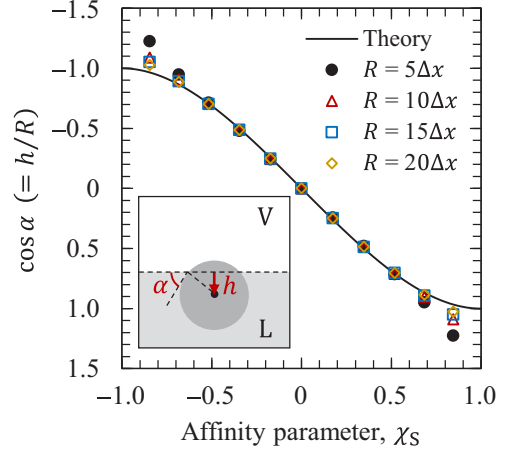


FIG. 3. Simulation results (filled circles) and theoretical estimations (solid line) for system B (see Table I): the values of  $\cos \alpha (=h/R)$ , where  $h$  is the downward distance from the liquid-vapor interface to the center of the particle, as shown in the inset, as a function of the affinity parameter  $\chi_S$  defined by Eq. (43) for  $R = 5\Delta x$ ,  $10\Delta x$ ,  $15\Delta x$ , and  $20\Delta x$ .

of the simulation cell, and then allowed to move toward a mechanically equilibrated position.

At the mechanically equilibrated state, the liquid-vapor interface capturing the wettable particle is not deformed, but remains horizontally flat because of the absence of gravity. The contact angle  $\alpha$  of the particle is given by

$$\cos \alpha = \frac{h}{R}, \quad (59)$$

where  $h$  is the downward distance from the liquid-vapor interface to the center of the particle, as shown in the inset of Fig. 3. Throughout this paper, the spatial location of the interface is defined as a series of positions giving  $\rho(x) = (\rho_L + \rho_V)/2$ .

Figure 3 shows  $\cos \alpha$  as a function of the affinity parameter  $\chi_S$  for a particle with four different radii ( $R = 5\Delta x$ ,  $10\Delta x$ ,  $15\Delta x$ , and  $20\Delta x$ ), demonstrating that the simulation results agree well with the theoretical estimation given by Eq. (43). Although the discrepancies between the simulation results and theoretical values appear as  $\chi_S$  approaches  $\pm 1$ , especially for the case of  $R = 5\Delta x$ , they are significantly reduced by employing the larger particles (namely, the resolution of a particle). This result is explained by the requirement for the particle radius,  $R > \max(4.164\xi_{LV}, \xi_{SP}) = 7.54\Delta x$ . Henceforth, in this study, the particle size is set to  $R = 10\Delta x$  judging from a balance between the computational accuracy and efficiency. Our model can represent a wide range of wettability values on the particle surface by tuning the affinity parameter  $\chi_S$ .

### C. Single particle adsorbed to the liquid-vapor interface in the presence of gravity

We now consider system C in Table I, where a wettable particle is trapped at a liquid-vapor interface in the presence of gravity. A circular particle of radius  $R$ , mass density  $\rho_P$ , and contact angle  $\alpha$  was initially placed at the center of the simulation cell, and then allowed to move toward a

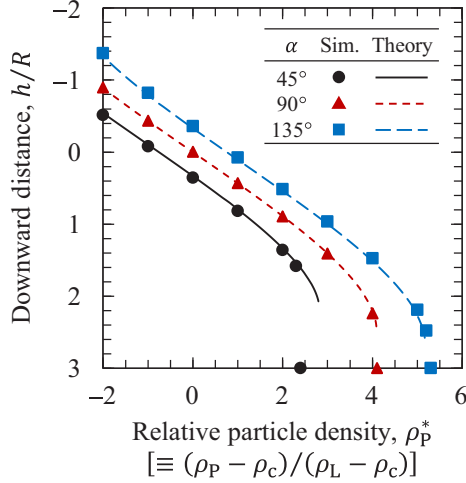


FIG. 4. Downward distance from the interface to the particle center,  $h/R$ , as a function of the relative particle density  $\rho_p^*$  [Eq. (57)] for system C (see Table I). The filled symbols and lines represent the simulation results and theoretical estimations, respectively, for contact angles of  $\alpha = 45^\circ$ ,  $90^\circ$ , and  $135^\circ$ . The plots corresponding to cases in which the particle separates from the liquid-vapor interface and falls down are depicted at the bottom of the graph.

mechanically equilibrated position, in which the particle weight was balanced with the force from the interfacial tension and the buoyancy force (caused by the asymmetric hydrostatic pressure). Regardless of particle wettability, for small relative densities  $\rho_p^*$  [Eq. (57)], the liquid-vapor interface around the particle is pushed upward (i.e., liquid level around the particle is higher than that for a horizontally flat interface) because the buoyancy force acting on the particle is greater than its weight. With an increase in  $\rho_p^*$ , the upward distortion reduces to form a horizontally flat liquid-vapor interface, and then the interface becomes distorted downward (i.e., liquid level around the particle is lower than that for a horizontally flat interface). Finally, the particle separates from the interface and falls down.

Figure 4 shows the downward distance from the interface to the particle center at the mechanically equilibrated state,  $h$ , as a function of  $\rho_p^*$  for contact angles of  $\alpha = 45^\circ$ ,  $90^\circ$ , and  $135^\circ$ , where the plots corresponding to cases in which the particle separates from the liquid-vapor interface are depicted at the bottom. Regardless of particle wettability, the downward distance  $h$  monotonically decreases with increasing  $\rho_p^*$ , and particles with larger values of  $\alpha$  remain in contact with the interface at larger values of  $\rho_p^*$ .

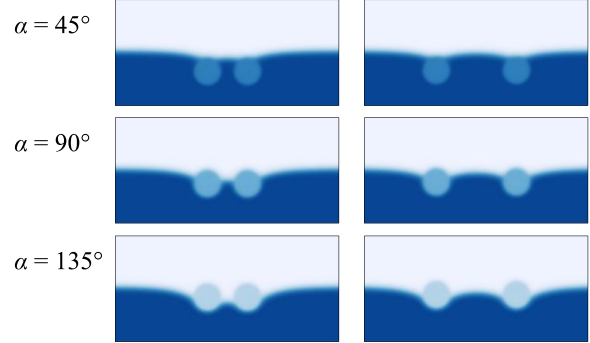
In Fig. 4, the simulation results for  $h$  are compared with the theoretical estimations from Eq. (A19) in Sec. 2 of the Appendix. They agree well with each other over a wide range of  $\rho_p^*$  for every contact angle case. Therefore, our model can represent the dynamics of a particle adsorbed to the liquid-vapor interface in the presence of gravity. Note that accurate and stable computations of the particle motion at the liquid-vapor interface are impossible without exact treatment of the gravitational force acting on the artificial fluid within the particle domain [Eq. (4)].

(a) Sample result  
(for system D.1 with  $\alpha = 135^\circ$  and  $L = 28\Delta x$ )

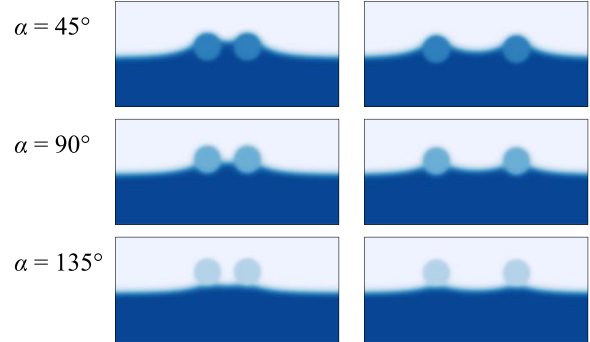


(b) System D.1

$L = 28\Delta x (\approx 2q^{-1})$        $L = 56\Delta x (\approx 4q^{-1})$



(c) System D.2



(d) System D.3



FIG. 5. (a) A typical snapshot of the simulations for system D (corresponding to system D.1 with  $\alpha = 135^\circ$  and  $L = 28\Delta x$ ) in a mechanically equilibrated state. (b)–(d) Enlarged snapshots of systems D.1–D.3 (see Table I) in a mechanically equilibrated state: (b) system D.1, two heavy (relative to the bulk fluids) particles with  $\rho_{p1}^* = \rho_{p2}^* = 2.0$  and (c) system D.2, two light (relative to the bulk fluids) particles with  $\rho_{p1}^* = \rho_{p2}^* = -2.0$ , where the contact angles are  $\alpha_1 = \alpha_2 = 45^\circ$ ,  $90^\circ$ , and  $135^\circ$ ; (d) system D.3, two particles with  $\rho_{p1}^* = 2.0$  and  $\rho_{p2}^* = -2.0$ , where the contact angles are  $\alpha_1 = 135^\circ$  and  $\alpha_2 = 45^\circ$ , respectively. The panels of the left- and right-hand sides display snapshots at horizontal center-to-center distances of  $L = 28\Delta x (\approx 2q^{-1})$  and  $56\Delta x (\approx 4q^{-1})$ , respectively.

#### D. Capillary flotation force: Two freely moving particles at the liquid-vapor interface in the presence of gravity

Let us consider system D in Table I, where two wettable particles trapped at a liquid-vapor interface freely move in the presence of gravity. A typical snapshot of the simulations in a mechanically equilibrated state is shown in Fig. 5(a) (corresponding to system D.1 with  $\alpha = 135^\circ$  and  $L = 28\Delta x$ ).



Firstly, we consider three cases: Fig. 5(b) shows system D.1, consisting of two heavy particles relative to the bulk fluids; Fig. 5(c) shows system D.2, consisting of two light particles relative to the bulk fluids; and Fig. 5(d) shows system D.3, consisting of one heavy particle and one light particle. Two circular particles of radius  $R$  and mass density  $\rho_{p_i}$  were initially placed with a contact angle of  $\alpha_i$  ( $i = 1$  or  $2$ ) on a flat liquid-vapor interface such that their horizontal center-to-center distance was  $L$  ( $< L_x/2$ ). The two particles were then allowed to move in the vertical direction under gravity toward their mechanically equilibrated positions, in which the particle weight was balanced with the buoyancy force (from the asymmetric hydrostatic pressure) and the force caused by interfacial tension.

Figures 5(b) and 5(c) show snapshots of systems D.1 and D.2, respectively, with contact angles of  $\alpha_1 = \alpha_2 = 45^\circ$ ,  $90^\circ$ , and  $135^\circ$  at the mechanically equilibrated states, while Fig. 5(d) shows snapshots of system D.3 at the mechanically equilibrated states. In Fig. 5, the two horizontal panels correspond to center-to-center distances of  $L = 28\Delta x$  ( $\approx 2q^{-1}$ ) and  $56\Delta x$  ( $\approx 4q^{-1}$ ). Regardless of the particle weight combination and interparticle distance, the heavy particles with  $\rho_{p_i}^* = 2.0$  push the liquid-vapor interface down, whereas the light particles with  $\rho_{p_i}^* = -2.0$  pull it up. This behavior is determined by the balance between the particle weight and the buoyancy force acting on the particle.

For systems D.1 [Fig. 5(b)] and D.2 [Fig. 5(c)], the vertical distance of the particle centers from the liquid-vapor interface increases in magnitude as the separation distance  $L$  decreases. Furthermore, in system D.1 (resp., D.2), the interface is less distorted for smaller (resp., larger) contact angles, because particles with higher (resp., lower) wettability are immersed more deeply into the liquid (resp., vapor), and are thus subject to a larger (resp., smaller) buoyancy force. In contrast, for system D.3 [Fig. 5(d)], the vertical distance of each particle center from the interface decreases in magnitude as  $L$  decreases. These results are illustrated quantitatively in Fig. 6(a), where  $h = h_1 = h_2 > 0$  for system D.1,  $h = h_1 = h_2 < 0$  for system D.2, and  $h = h_1 = -h_2 > 0$  for system D.3. The simulation results for  $h$  agree well with the theoretical estimations from Eqs. (A5) and (A12) in Sec. 1 of the Appendix.

In the horizontal direction, the forces created by interfacial tension and hydrostatic pressure are unbalanced, resulting in a lateral force between the two particles at the liquid-vapor interface,  $F_{\text{lat}}$ , which is referred to as the capillary flotation force. For every calculation,  $F_{\text{lat}}$  is presented as a function of the separation distance  $L$  in Fig. 6(b), where the sign of  $F_{\text{lat}}$  is defined such that attractive forces have negative values. The forces are attractive for all values of  $\alpha$  in systems D.1 and D.2, whereas they are repulsive for system D.3. In every system, the forces become stronger with decreasing  $L$ , a result of the increase in the degree of interface distortion around the particles (Fig. 5). In Fig. 6(b), the simulation results for  $F_{\text{lat}}$  are compared with the theoretical estimations from Eq. (A2) in Sec. 1 of the Appendix, demonstrating that our simulation results agree well with the theoretical estimations for various density combinations and particle wettabilities.

The force-distance profile [Fig. 6(b)] is recast as a semilogarithmic graph in Fig. 6(c), demonstrating that, regardless of particle density combination and wettability, the lateral forces

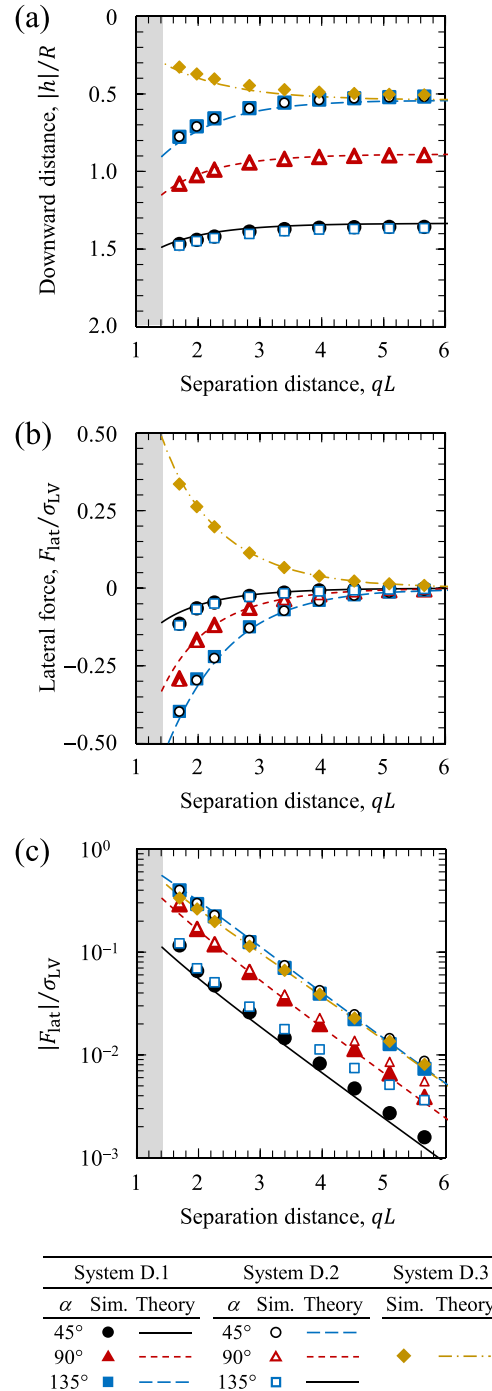


FIG. 6. Simulation results (symbols) and theoretical estimations (lines) for system D (see Table I): (a) absolute value of downward distance  $|h|$  and (b) capillary flotation force  $F_{\text{lat}}$  as a function of the separation distance  $L$  for systems D.1 and D.2 with contact angles of  $\alpha = 45^\circ$ ,  $90^\circ$ , and  $135^\circ$ , and for system D.3; (c) semilogarithmic graph obtained from the force-distance profile in (b). In panel (a),  $h = h_1 = h_2 > 0$  for system D.1,  $h = h_1 = h_2 < 0$  for system D.2, and  $h = h_1 = -h_2 > 0$  for system D.3. In panel (b), the sign of  $F_{\text{lat}}$  is defined such that attractive forces have negative values. In all panels, the theoretical lines for system D.1 with  $\alpha = 45^\circ$  and system D.2 with  $\alpha = 135^\circ$ , for systems D.1 and D.2 with  $\alpha = 90^\circ$ , and for system D.1 with  $\alpha = 135^\circ$  and system D.2 with  $\alpha = 45^\circ$  are identical.

TABLE II. Decay lengths  $\lambda$  obtained by fitting the exponential decay function  $|F| \sim \exp(-L/\lambda)$  to the simulation data for  $qL > 2.2$  in Fig. 6(c).

System	$\alpha = 45^\circ$	$\alpha = 90^\circ$	$\alpha = 135^\circ$	$\alpha_1 = 45^\circ, \alpha_2 = 135^\circ$
D.1	$14.1\Delta x$	$14.0\Delta x$	$14.1\Delta x$	
D.2	$14.7\Delta x$	$15.4\Delta x$	$18.2\Delta x$	
D.3				$15.0\Delta x$

decrease exponentially with a decay length of  $\lambda$ . Fitting an exponential decay function of  $|F| \sim \exp(-L/\lambda)$  to the simulation data for  $qL > 2.2$ , in which the theoretical lines are approximately  $|F_{\text{lat}}/\sigma_{\text{LV}}| \sim \exp(-qL)$ , the decay lengths  $\lambda$  for all cases are summarized in Table II. The decay lengths  $\lambda$  are in good agreement with the capillary length of  $q^{-1} = 14.1\Delta x$ , except for system D.2 with  $\alpha = 135^\circ$ , in which the value of  $|F_{\text{lat}}/\sigma_{\text{LV}}|$  is relatively small. Therefore, our model can represent the capillary flotation forces between two particles at the liquid-vapor interface in the presence of gravity. Note that discrepancies between the simulations and theoretical results appear at  $qL \approx 1.7$ . This is likely to have been caused by the overlap between the two wetting layers formed around the particles. One simple way to diminish the influence of the overlap is to use larger particles. More detailed examinations, as well as improvements to the proposed model, will be the focus of future work.

As an additional demonstration of the proposed model, we considered system D.4, where two particles were initially located in the vapor phase and then allowed to fall downward in the presence of gravity. Two circular particles with  $R = 10\Delta x$ ,  $\alpha_1 = \alpha_2 = 90^\circ$ , and relative mass density of  $\rho_{\text{P}1}^* = \rho_{\text{P}2}^*$  were initially placed at the vapor phase ( $y = 70.5\Delta x$ ), where their horizontal center-to-center distance was  $L = 40\Delta x$ . The two particles were then allowed to move freely in all directions under gravity.

The snapshots of system D.4 for  $\rho_{\text{P}1}^* = \rho_{\text{P}2}^* = 2.0$  and 5.0 are displayed in Figs. 7(a) and 7(b), respectively, and the trajectories of particles 1 and 2 during  $1 \times 10^6$  time steps are depicted in Fig. 7(c). The two particles move downward as in Fig. 7(c) and push the liquid-vapor interface down (a1, b1). In the case of  $\rho_{\text{P}1}^* = \rho_{\text{P}2}^* = 2.0$ , the particles are captured by the interface to approach each other due to the capillary flotation force (a2,c) and finally rest at their mechanically equilibrated positions (a3,c), where the fluid-induced capillary flotation force  $F_k^{\text{H}}$  in Eq. (4) is in balance with, horizontally, the direct particle-particle interaction force  $F_k^{\text{P}}$  and with, vertically, the gravitational force  $F_k^{\text{G}}$  for each particle ( $k = 1$  and 2). On the other hand, the heavier particles with  $\rho_{\text{P}1}^* = \rho_{\text{P}2}^* = 5.0$  are temporally captured at the liquid-vapor interface during the time steps from  $1.0 \times 10^4$  to  $13.5 \times 10^4$  (b2,c) and eventually fall away from the interface (b3,c). The interfacial attachment or detachment behavior of two particles of  $\rho_{\text{P}1}^* = \rho_{\text{P}2}^* = 2.0$  or 5.0 is in good agreement with that of a single particle (Fig. 4 for  $\alpha = 90^\circ$ ). Figure 7(c) demonstrates that the particles move smoothly in all directions for both cases of  $\rho_{\text{P}1}^* = \rho_{\text{P}2}^* = 2.0$  and 5.0. In addition, it was confirmed that the mass conservation for the liquid and vapor phases was satisfied during the particles' motion, with negligible errors. Therefore, the

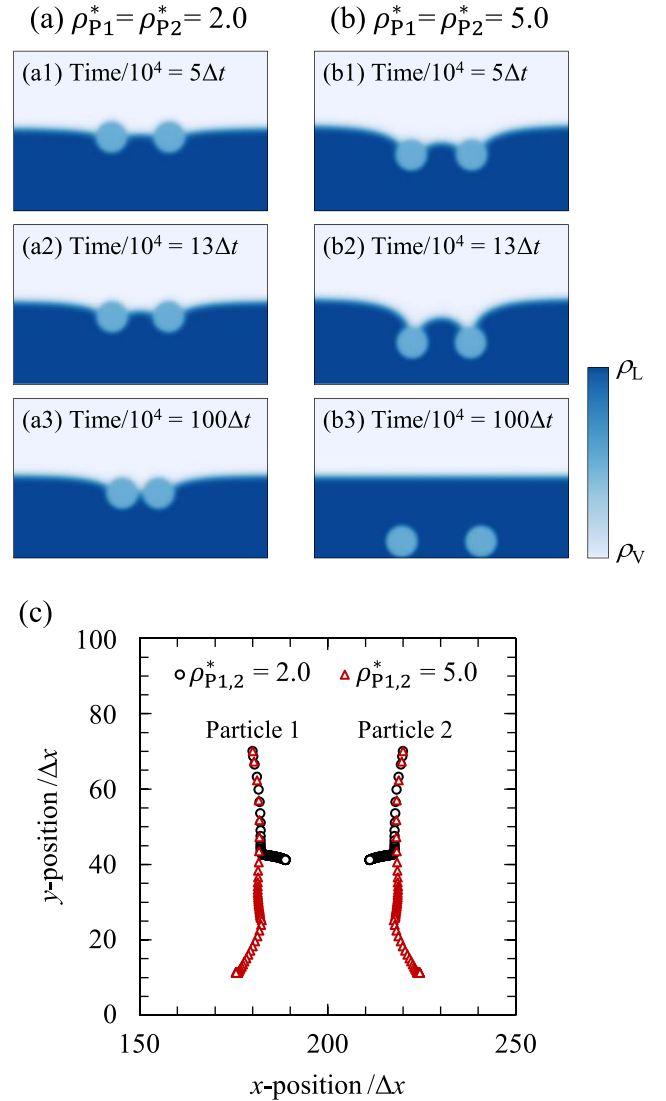


FIG. 7. Simulation results for system D.4 (see Table I), where two particles initially located in the vapor phase were allowed to move freely in all directions under gravity. (a), (b) Time series snapshots for particles with  $\rho_{\text{P}1}^* = \rho_{\text{P}2}^* = 2.0$  (a) and  $\rho_{\text{P}1}^* = \rho_{\text{P}2}^* = 5.0$  (b). (c) The trajectories of the particles 1 and 2 with  $\rho_{\text{P}1}^* = \rho_{\text{P}2}^* = 2.0$  (black open circles) and  $\rho_{\text{P}1}^* = \rho_{\text{P}2}^* = 5.0$  (red open triangles) during  $1 \times 10^6$  time steps, where the positions of the particles are shown every 5000 time steps.

proposed model can provide stable simulations of particle dynamics at a liquid-vapor interface under gravity.

### E. Capillary immersion force: Two vertically constrained particles at the liquid-vapor interface in the presence of gravity

Let us consider system E in Table I, where two identical particles trapped at a liquid-vapor interface are vertically constrained and move in the horizontal direction only in the presence of gravity. Although system E is similar to system D, it exhibits different phenomena. Such a situation can be seen, for example, when particles are in contact with a solid substrate covered with a thin liquid film in a vapor phase

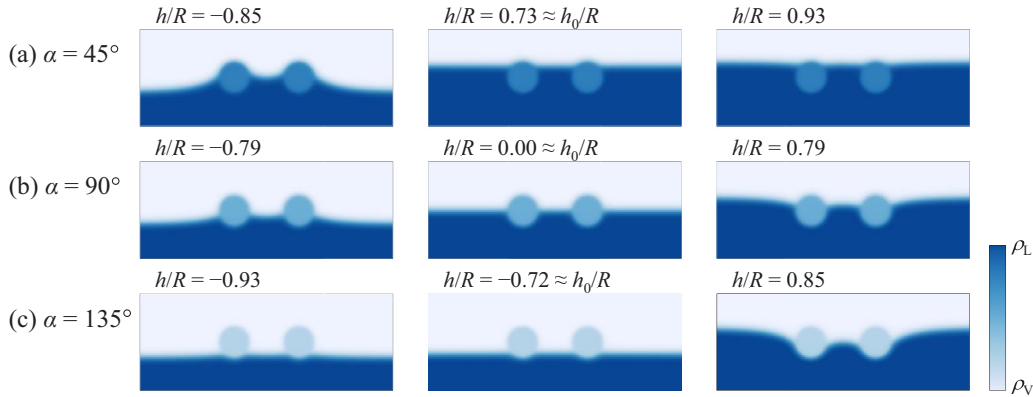


FIG. 8. Snapshots for the simulations of system E (see Table I) with contact angles of (a)  $\alpha = 45^\circ$ , (b)  $\alpha = 90^\circ$ , and (c)  $\alpha = 135^\circ$  in mechanically equilibrated state. For every panel, from left to right, the snapshots correspond to downward distances of  $h < h_0$ ,  $h \approx h_0$ , and  $h > h_0$ , where  $h_0 \equiv R \cos \alpha$ .

[7,38]. Simulations of system E were conducted in the same way as those of system D, except for the following points. Two identical circular particles with a radius of  $R$  and a contact angle of  $\alpha_1 = \alpha_2 = \alpha$  were constrained at the vertical position  $y = L_y/2$  with a horizontal center-to-center distance of  $L = 4R$ . The area fraction of the liquid phase was varied in the range 0.4–0.6, resulting in different downward distances  $h_1 = h_2 = h$  at the mechanically equilibrated states.

Figure 8 shows snapshots of particles with  $\alpha = 45^\circ$  [Fig. 8(a)],  $90^\circ$  [Fig. 8(b)], and  $135^\circ$  [Fig. 8(c)] at the mechanically equilibrated states, where the three horizontal panels correspond to different values of  $h$ . Regardless of contact angle  $\alpha$ , the liquid-vapor interfaces around the two particles remain horizontally flat for  $h/R \approx h_0/R \equiv \cos \alpha = 0.707$ , 0, and  $-0.707$  for  $\alpha = 45^\circ$ ,  $90^\circ$ , and  $135^\circ$ , respectively. The liquid-vapor interfaces deform to be concave upward and downward for  $h < h_0$  (i.e., the liquid level is lower than that for a horizontally flat interface) and  $h > h_0$ , (i.e., the liquid level is higher than that for a horizontally flat interface), respectively.

In the horizontal and vertical directions, the forces created by the interfacial tension and the hydrostatic pressure are unbalanced. This results in a lateral force between the two particles at the liquid-vapor interface,  $F_{\text{lat}}$ , which is referred to as the capillary immersion force, and a vertical force acting on each of the particles,  $F_{\text{ver}}$ . The forces  $F_{\text{lat}}$  and  $F_{\text{ver}}$  are displayed as a function of  $h$  in Figs. 9(a) and 9(b), respectively. In Fig. 9(a), for each contact angle  $\alpha$ , the lateral force  $F_{\text{lat}}$  is almost zero at  $h \approx h_0$ , where the interface is horizontally flat, as shown in the middle panel of Fig. 8. For  $h < h_0$  and  $h > h_0$ ,  $F_{\text{lat}}$  is an attractive force, and increases with increasing  $|h - h_0|$ . In contrast,  $F_{\text{ver}}$  acts upward and monotonically increases in magnitude with increasing  $h$ .

It is apparently unnatural for the vertical force  $F_{\text{ver}}$  to act upward regardless of  $h$ . However, this is because  $F_{\text{ver}}$  contains the buoyancy force from the asymmetric hydrostatic pressure. As described in Sec. 3 of the Appendix,  $F_{\text{ver}}$  consists of the force created by interfacial tension  $F_{\text{ver}}^\sigma$  [Eq. (A21)] and the buoyancy force  $F_{\text{ver}}^b$  [Eq. (A22)], the theoretical values of which are displayed in Fig. 9(c). For each contact angle  $\alpha$ ,  $F_{\text{ver}}^\sigma$  is almost zero at  $h \approx h_0$ , where the interface is horizontally flat, as shown in the middle panel of Fig. 8. For  $h < h_0$  and

$h > h_0$ ,  $F_{\text{ver}}^\sigma$  acts downward and upward, respectively, increasing in magnitude with an increase in  $|h - h_0|$ .

The simulation results for  $F_{\text{lat}}$  and  $F_{\text{ver}}$  are compared with the theoretical estimations (see Sec. 3 of the Appendix) in Figs. 9(a) and 9(b), respectively. For every contact angle, our simulation results agree well with the theoretical estimations. This demonstrates that our model can capture the lateral capillary forces between two particles at the liquid-vapor interface.

#### IV. CONCLUSION

We have developed a computational method for simulating wettable particles adsorbed to a liquid-vapor interface under gravity. The proposed method combines the iSPLBM and free-energy LBM for a liquid-vapor system. To confirm the performance of this model, we examined five benchmark two-dimensional problems.

The capillary flotation forces between two particles were found to be attractive for two identical heavy or light particles, but repulsive in the system containing one heavy and one light particle. These forces became stronger as the separation distance between the particles decreased because of the larger distortion of the liquid-vapor interface around the particles. The capillary immersion forces were found to be attractive and to increase with increasing curvature of the liquid-vapor interfaces in the case of a fixed separation distance between the particles. The simulation results were also shown to be in good quantitative agreement with theoretical estimations and to be stable for calculations of dynamics of particles with various densities around the interfaces.

The proposed method can reproduce the capillary interactions between wettable particles at a liquid-vapor interface under gravity. This method now can treat the systems with the small density contrast between the liquid and vapor phases due to the description of a two-phase fluid with the fundamental free-energy model proposed by Swift *et al.* [25]. Recently, some advanced models were proposed to treat the two-phase fluid system with large density ratio (e.g., Refs. [39,40]) within the framework of free-energy models. Because our proposed model is simple and preserves physical and thermodynamic consistencies, the methodology of the proposed

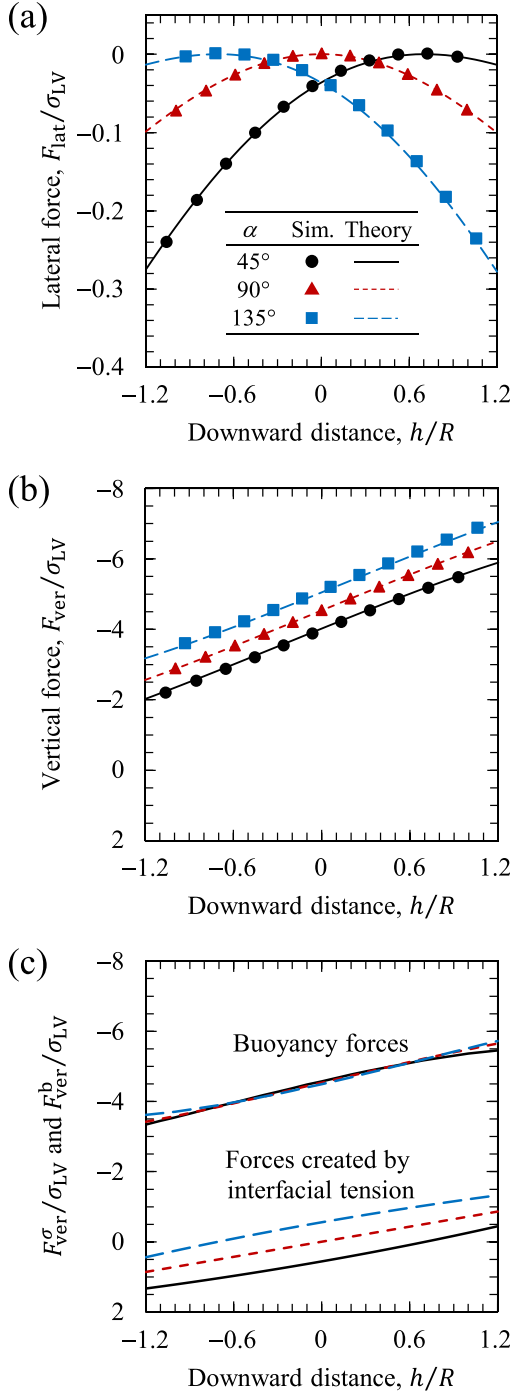


FIG. 9. Simulation results (filled symbols) and theoretical estimations (lines) for system E (see Table I) in a mechanically equilibrated state. (a) Capillary immersion force  $F_{\text{lat}}$ , (b) vertical force  $F_{\text{ver}}$ , and (c) contributions of the interfacial tension,  $F_{\text{ver}}^\sigma$ , and buoyancy force,  $F_{\text{ver}}^b$ , to the vertical force as a function of  $h$ . The lines in panels (a), (b) represent the theoretical estimations from Eqs. (A2) and (A20), and the lines for the force from interfacial tension and the buoyancy force in panel (c) represent the theoretical estimations from Eqs. (A21) and (A22), respectively.

model can be applied to the advanced models with minor modifications.

## ACKNOWLEDGMENTS

This work was supported by JSPS KAKENHI (Grants No. JP20K15075 and No. JP18H03690) and by The Information Center of Particle Technology, Japan.

## APPENDIX

Theoretical expressions of the capillary flotation force and the capillary immersion force were reported in Refs. [35] and [36], respectively. For the sake of consistency, this Appendix provides theoretical descriptions of systems C, D.1–D.3, and E based on these references.

### 1. Capillary flotation force: Two freely moving particles at liquid-vapor interface in the presence of gravity (systems D.1–D.3)

We set systems D.1–D.3 as illustrated in Fig. 10, consisting of two wettable circular particles  $i$  ( $=1$  or  $2$ ) with a radius of  $R$ , mass density of  $\rho_{\text{Pi}}$ , contact angle of  $\alpha_i$ , and horizontal center-to-center distance between the particles of  $L$ . The particles float at the liquid-vapor interface in the presence of gravity. The level of the undisturbed horizontal interface far from the particles defines the origin of the vertical axis  $z$ ;  $r$  is the current variable along the horizontal axis.

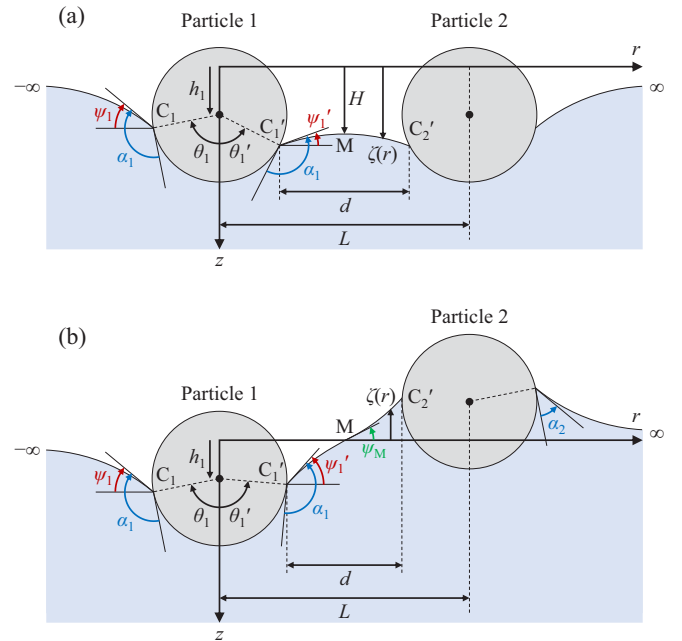


FIG. 10. Schematic illustrations of systems D.1–D.3 (see Table I) in a mechanically equilibrated state, where two freely moving particles  $i$  ( $=1$  or  $2$ ) with the same radius of  $R$ , relative density of  $\rho_{\text{Pi}}^*$ , contact angle of  $\alpha_i$ , and a horizontal center-to-center distance of  $L$  float at a liquid-vapor interface in the presence of gravity: (a) two identical particles (systems D.1 and D.2); (b) two particles with different mass density and wettability (system D.3). In system D.3, for the sake of simplification, the heavy particle has  $\rho_{\text{P1}}^*$  and  $\alpha_1$  and the light particle has  $\rho_{\text{P2}}^* = -\rho_{\text{P1}}^*$  and  $\alpha_2 = 180^\circ - \alpha_1$ . The other mathematical symbols are explained in the main text.

The vertical positions of the center of particle  $i$  and the apex M of the interior meniscus between the particles are  $h_i$  and  $H$ , respectively. The vertical positions of the three-phase contact points  $C_i$  and  $C'_i$ , which are characterized by angles of  $\theta_i$  and  $\theta'_i$ , are expressed by  $h_i + R \cos \theta_i$  and  $h_i + R \cos \theta'_i$ , respectively. The slope angles of the exterior and interior menisci are  $\psi_i (\equiv \alpha_i + \theta_i - \pi)$  and  $\psi'_i (\equiv \alpha_i + \theta'_i - \pi)$ , respectively.

Each floating particle is subjected to the gravitational force (i.e., its weight), the force from the asymmetrical hydrostatic pressure (i.e., buoyancy force), and the force created by interfacial tension. At the equilibrated state, the vertical force balance on particle 1 is given by

$$\text{Bo} \left[ \theta_1 + \theta'_1 + \sin \theta_1 \cos \theta_1 + \sin \theta'_1 \cos \theta'_1 + \frac{2h_1}{R} (\sin \theta_1 + \sin \theta'_1) \right] = 2[\sin(\alpha_1 + \theta_1) + \sin(\alpha_1 + \theta'_1) + \pi \text{Bo} D_1], \quad (\text{A1})$$

where Bo is the Bond number, which is defined by Eqs. (55) and (56), and  $D_1 \equiv (\rho_{P1} - \rho_V)/(\rho_L - \rho_V)$ . The lateral interaction force acting on particle 1,  $F_{\text{lat}}$ , is expressed by

$$F_{\text{lat}} = -\sigma_{\text{LV}} [\cos(\alpha_1 + \theta_1) - \cos(\alpha_1 + \theta'_1)] - \text{Bo} \sigma_{\text{LV}} \left[ \frac{1}{2} (\sin^2 \theta_1 - \sin^2 \theta'_1) + \frac{h_1}{R} (\cos \theta'_1 - \cos \theta_1) \right]. \quad (\text{A2})$$

The shape of the interface around the particles obeys the Laplace capillary equation [7],

$$\frac{d}{dr} \left[ \frac{d\zeta/dr}{\sqrt{1 + (d\zeta/dr)^2}} \right] = \frac{(\rho_L - \rho_V)g\zeta}{\sigma_{\text{LV}}}, \quad (\text{A3})$$

where  $z = \zeta(r)$  is the equation of the deformed fluid interface. Taking the interface shape  $\zeta$  and its slope  $\psi$  as variables, Eq. (A3) yields the parametrized form [7]:

$$-\frac{d(\cos \psi)}{d\zeta} = q^2 \zeta. \quad (\text{A4})$$

#### a. Two identical particles (systems D.1 and D.2)

Two circular particles with the same density, i.e.,  $\rho_{P1} = \rho_{P2}$ , and the same contact angle, i.e.,  $\alpha_1 = \alpha_2$ , are considered, as shown in Fig. 10(a). In this case, there is a plane of reflection symmetry midway between the two particles. After integrating Eq. (A4) from  $-\infty$  ( $\zeta = 0$ ,  $\psi = 0$ ) to  $C_1$  ( $\zeta = h_1 + R \cos \theta_1$ ,  $\psi = \psi_1$ ) and from  $C'_1$  ( $\zeta = h_1 + R \cos \theta'_1$ ,  $\psi = \psi'_1$ ) to M ( $\zeta = H$ ,  $\psi = 0$ ), we obtain the conditions for interfacial equilibrium:

$$\text{Bo} \left( \frac{h_1}{R} + \cos \theta_1 \right)^2 = 2[1 + \cos(\alpha_1 + \theta_1)], \quad (\text{A5})$$

$$\text{Bo} \left[ \left( \frac{h_1}{R} + \cos \theta'_1 \right)^2 - \left( \frac{H}{R} \right)^2 \right] = 2[1 + \cos(\alpha_1 + \theta'_1)]. \quad (\text{A6})$$

The solution of Eq. (A4) under the condition  $\zeta = H$ ,  $\psi = 0$  is

$$q\zeta = [(qH)^2 + 2(1 - \cos \psi)]^{1/2}. \quad (\text{A7})$$

Combining Eq. (A7) with the relation  $d\zeta/dr = -\tan \psi$  leads to

$$\frac{d(qr)}{d\psi} = -\frac{\cos \psi}{[(qH)^2 + 2(1 - \cos \psi)]^{1/2}}. \quad (\text{A8})$$

Integrating Eq. (A8) from  $C'_1$  to M yields the dimensionless horizontal distance between the three-phase lines  $C'_1$  and  $C'_2$  of the interior meniscus:

$$qd = \frac{2}{a} \left\{ (2 - a^2) \left[ F\left(a, \frac{\pi}{2}\right) - F\left(a, \frac{\pi - |\psi'_1|}{2}\right) \right] - 2 \left[ E\left(a, \frac{\pi}{2}\right) - E\left(a, \frac{\pi - |\psi'_1|}{2}\right) \right] \right\}, \quad (\text{A9})$$

where

$$a^2 = \frac{4}{4 + (qH)^2}. \quad (\text{A10})$$

In Eq. (A9),  $F(a, \phi)$  and  $E(a, \phi)$  are elliptic integrals of the first and second kind with modulus  $a$  and amplitude  $\phi$  [41]. The center-to-center distance between the two particles is given by

$$qL = qd + 2\text{Bo}^{1/2} \sin \theta'_1. \quad (\text{A11})$$

This set of equations is solved numerically as follows. First, angle  $\theta'_1$  is specified;  $\theta_1$  and  $h_1$  are then calculated by Eqs. (A1) and (A5) with the condition that  $h_1 + R \cos \theta_1$  has the same sign as  $\psi_1$ .  $H$  is calculated by Eq. (A6) with the condition that  $h_1 + R \cos \theta'_1$  has the same sign as  $\psi'_1$ . Finally, the lateral interaction force  $F_{\text{lat}}$ , the distance between the three-phase contact points  $d$ , and the center-to-center distance between the particles  $L$  are calculated using Eqs. (A2), (A9), and (A11), respectively.

#### b. Two particles with different mass density and wettability (system D.3)

For the sake of simplification, we consider a heavy particle with  $\rho_{P1}^*$  and  $\alpha_1$  and a light particle with  $\rho_{P2}^* = -\rho_{P1}^*$  and  $\alpha_2 = 180^\circ - \alpha_1$ , as shown in Fig. 10(b). In this case, the meniscus has an inflection point at M ( $r = L/2$ ,  $\zeta = 0$ ), where the meniscus slope  $\psi = \psi_M$ : the meniscus is symmetrical with respect to the inflection point, i.e.,  $\psi'_2 = -\psi'_1$  or  $\theta'_2 = 180^\circ - \theta'_1$  [36].

After integrating Eq. (A4) from  $-\infty$  ( $\zeta = 0$ ,  $\psi = 0$ ) to  $C_1$  ( $\zeta = h_1 + R \cos \theta_1$ ,  $\psi = \psi_1$ ) and from  $C'_1$  ( $\zeta = h_1 + R \cos \theta'_1$ ,  $\psi = \psi'_1$ ) to M ( $\zeta = 0$ ,  $\psi = \psi_M$ ), we obtain the conditions for interfacial equilibrium:

$$\text{Bo} \left( \frac{h_1}{R} + \cos \theta_1 \right)^2 = 2[1 + \cos(\alpha_1 + \theta_1)], \quad (\text{A12})$$

$$\text{Bo} \left( \frac{h_1}{R} + \cos \theta'_1 \right)^2 = 2[\cos \psi_M + \cos(\alpha_1 + \theta'_1)]. \quad (\text{A13})$$

The solution of Eq. (A4) under the condition  $\zeta = 0$ ,  $\psi = \psi_M$  is

$$q\zeta = 2[\cos^2(\psi_M/2) - \cos^2(\psi/2)]^{1/2}. \quad (\text{A14})$$

Combining Eq. (A14) with the relation  $d\zeta/dr = -\tan\psi$  leads to

$$\frac{d(qr)}{d(\psi/2)} = -\frac{1 - 2\sin^2(\psi/2)}{[\cos^2(\psi_M/2) - \cos^2(\psi/2)]^{1/2}}. \quad (\text{A15})$$

Integrating Eq. (15) from  $C'_1$  to M yields the dimensionless horizontal distance between the three-phase contact points  $C'_1$  and  $C'_2$  of the interior meniscus:

$$qd = 2\left[F\left(b, \frac{\pi}{2}\right) - F(b, \phi'_1)\right] - 4\left[E\left(b, \frac{\pi}{2}\right) - E(b, \phi'_1)\right], \quad (\text{A16})$$

where

$$b = \cos(\psi_M/2), \quad \sin\phi'_1 = \frac{\cos(\psi'_1/2)}{\cos(\psi_M/2)}. \quad (\text{A17})$$

The center-to-center distance between the two particles  $L$  is given by Eq. (A11).

This set of equations is solved numerically as follows. First, angle  $\theta'_1$  is specified;  $\theta_1$  and  $h_1$  are then calculated by Eqs. (A1) and (A12) with the condition that  $h_1 + R\cos\theta_1$  has the same sign as  $\psi_1$ .  $\psi_M$  is calculated by Eq. (A13) with the condition that  $h_1 + R\cos\theta'_1$  has the same sign as  $\psi'_1$ . Finally, the lateral interaction force  $F_{\text{lat}}$ , the distance between the three-phase contact points  $d$ , and the center-to-center distance between the particles  $L$  are calculated using Eqs. (A2), (A16), and (A11), respectively.

## 2. Single particle adsorbed to liquid-vapor interface in the presence of gravity (system C)

For a theoretical description of an isolated circular particle, we can consider the situation in which the center-to-center distance between the particles is infinite;  $\theta_1 = \theta'_1 = \theta_0$  and  $H = 0$ . Incorporating these values into Eq. (A1) leads to

$$\text{Bo}\left[\theta_0 + \sin\theta_0 \cos\theta_0 + \frac{2h}{R} \sin\theta_0\right] = 2\sin(\alpha + \theta_0) + \pi\text{Bo}D, \quad (\text{A18})$$

and in the same manner, Eqs. (A5) and (A6) reduce to

$$\text{Bo}\left(\frac{h}{R} + \cos\theta_0\right)^2 = 2[1 + \cos(\alpha + \theta_0)]. \quad (\text{A19})$$

These equations are solved numerically, establishing the relations between the density parameter  $D$  and the vertical position of the center of the isolated particle  $h$ .

## 3. Capillary immersion force: Two vertically constrained particles at liquid-vapor interface in the presence of gravity (system E)

As shown in Fig. 10(a), system E consists of two identical particles with a radius of  $R$ , a contact angle of  $\alpha_1 = \alpha_2$ , and a horizontal center-to-center distance between the particles of  $L$ . The particles are constrained at the same vertical position, and  $h_i$ ,  $H$ ,  $\theta_i$ ,  $\theta'_i$ ,  $\psi_i$ , and  $\psi'_i$  ( $i = 1$  or  $2$ ) are defined in the same fashion as for system D. Hence, the formal expressions for system E are the same as those for system D [e.g., Eqs. (A2), (A5), (A6), and (A9)–(A11)], except for several expressions described below.

The lateral force  $F_{\text{lat}}$  acting on each particle is given by Eq. (A2), while the vertical force balance [Eq. (A1)] is replaced with an equation for the vertical force acting on the particle:

$$F_{\text{ver}} = -\frac{\text{Bo}\sigma_{\text{LV}}}{2}\left[\theta_1 + \theta'_1 + \sin\theta_1 \cos\theta_1 + \sin\theta'_1 \cos\theta'_1 + \frac{2h}{R}(\sin\theta_1 + \sin\theta'_1)\right] + \sigma_{\text{LV}}[\sin(\alpha + \theta_1) + \sin(\alpha + \theta'_1)] - \pi R^2 \rho_V g, \quad (\text{A20})$$

where  $F_{\text{ver}} > 0$  and  $F_{\text{ver}} < 0$  represent the downward and upward forces on each particle, respectively.

With the constant center-to-center distance of  $L$ , forces  $F_{\text{lat}}$  and  $F_{\text{ver}}$  are numerically obtained as a function of the vertical position of the central axis of the particles  $h_1$ . When  $h_1$  is specified,  $\theta_1$  is calculated by Eq. (A5) with the condition that  $h_1 + R\cos\theta_1$  has the same sign as  $\psi_1$ . If the value of  $\theta'_1$  is assigned,  $H$  is calculated by Eq. (A6) with the condition that  $h_1 + R\cos\theta'_1$  has the same sign as  $\psi'_1$ , and the distance between the three-phase contact points  $d$  and the center-to-center distance between the particles  $L$  are calculated from Eqs. (A9) and (A11), respectively. Therefore,  $\theta'_1$  is iteratively determined so that the resultant  $L$  converges to the set value. After successful convergence, the lateral force  $F_{\text{lat}}$  and the vertical force  $F_{\text{ver}}$  are calculated with Eqs. (A2) and (A20), respectively. From Eq. (A20), the contribution of the interfacial tension to the vertical force,  $F_{\text{ver}}^\sigma$ , is calculated as

$$F_{\text{ver}}^\sigma = \sigma_{\text{LV}}[\sin(\alpha + \theta_1) + \sin(\alpha + \theta'_1)], \quad (\text{A21})$$

and the buoyancy force  $F_{\text{ver}}^b$  is calculated as

$$F_{\text{ver}}^b = -\frac{\text{Bo}\sigma_{\text{LV}}}{2}\left[\theta_1 + \theta'_1 + \sin\theta_1 \cos\theta_1 + \sin\theta'_1 \cos\theta'_1 + \frac{2h}{R}(\sin\theta_1 + \sin\theta'_1)\right] - \pi R^2 \rho_V g. \quad (\text{A22})$$

- [1] N. B. Bowden, M. Weck, I. S. Choi, and G. M. Whitesides, Molecule-mimetic chemistry and mesoscale self-assembly, *Acc. Chem. Res.* **34**, 231 (2001).  
 [2] R. McGorty, J. Fung, D. Kaz, and V. N. Manoharan, Colloidal self-assembly at an interface, *Mater. Today* **13**, 34 (2010).  
 [3] L. Botto, E. P. Lewandowski, M. Cavallaro, and K. J. Stebe, Capillary interactions between anisotropic particles, *Soft Matter* **8**, 9957 (2012).

- [4] D. Zang, S. Tarafdar, Y. Y. Tarasevich, M. D. Choudhury, and T. Dutta, Evaporation of a droplet: From physics to applications, *Phys. Rep.* **804**, 1 (2019).  
 [5] L. E. Low, S. P. Siva, Y. K. Ho, E. S. Chan, and B. T. Tey, Recent advances of characterization techniques for the formation, physical properties and stability of Pickering emulsion, *Adv. Colloid Interface Sci.* **277**, 102117 (2020).

- [6] Y. Xing, X. Gui, L. Pan, B. E. Pinchasik, Y. Cao, J. Liu, M. Kappl, and H. J. Butt, Recent experimental advances for understanding bubble-particle attachment in flotation, *Adv. Colloid Interface Sci.* **246**, 105 (2017).
- [7] P. A. Kralchevsky and K. Nagayama, *Particles at Fluid Interfaces and Membranes* (Elsevier, Amsterdam, 2001).
- [8] G. Liang, Z. Zeng, Y. Chen, J. Onishi, H. Ohashi, and S. Chen, Simulation of self-assemblies of colloidal particles on the substrate using a lattice Boltzmann pseudo-solid model, *J. Comput. Phys.* **248**, 323 (2013).
- [9] M. Fujita, O. Koike, and Y. Yamaguchi, Direct simulation of drying colloidal suspension on substrate using immersed free surface model, *J. Comput. Phys.* **281**, 421 (2015).
- [10] S. Chen and G. D. Doolen, Lattice Boltzmann method for fluid flows, *Annu. Rev. Fluid Mech.* **30**, 329 (1998).
- [11] S. Succi, *The Lattice Boltzmann Equation for Fluid Dynamics and Beyond* (Oxford University Press, Oxford, 2001).
- [12] Q. Li, K. H. Luo, Q. J. Kang, Y. L. He, Q. Chen, and Q. Liu, Lattice Boltzmann methods for multiphase flow and phase-change heat transfer, *Prog. Energy Combust. Sci.* **52**, 62 (2016).
- [13] A. J. C. Ladd, Numerical simulations of particulate suspensions via a discretized Boltzmann equation. Part I. Theoretical foundation, *J. Fluid Mech.* **271**, 285 (1994).
- [14] D. R. Noble and J. R. Torczynski, A lattice-Boltzmann method for partially saturated computational cells, *Int. J. Mod. Phys. C* **9**, 1189 (1998).
- [15] Z. G. Feng and F. E. Michaelides, Proteus: A direct forcing method in the simulations of particulate flows, *J. Comput. Phys.* **202**, 20 (2005).
- [16] S. Jafari, R. Yamamoto, and M. Rahnama, Lattice-Boltzmann method combined with smoothed-profile method for particulate suspensions, *Phys. Rev. E* **83**, 026702 (2011).
- [17] K. Stratford, R. Adhikari, I. Pagonabarraga, and J. C. Desplat, Lattice Boltzmann for binary fluids with suspended colloids, *J. Stat. Phys.* **121**, 163 (2005).
- [18] J. Onishi, A. Kawasaki, Y. Chen, and H. Ohashi, Lattice Boltzmann simulation of capillary interactions among colloidal particles, *Comput. Math. Appl.* **55**, 1541 (2008).
- [19] A. S. Joshi and Y. Sun, Multiphase lattice Boltzmann method for particle suspensions, *Phys. Rev. E* **79**, 066703 (2009).
- [20] K. W. Connington, T. Lee, and J. F. Morris, Interaction of fluid interfaces with immersed solid particles using the lattice Boltzmann method for liquid-gas-particle systems, *J. Comput. Phys.* **283**, 453 (2015).
- [21] Y. K. Lee and K. H. Ahn, Particle dynamics at fluid interfaces studied by the color gradient lattice Boltzmann method coupled with the smoothed profile method, *Phys. Rev. E* **101**, 053302 (2020).
- [22] Y. Mino and H. Shinto, Lattice Boltzmann method for simulation of wettable particles at a fluid-fluid interface under gravity, *Phys. Rev. E* **101**, 033304 (2020).
- [23] Y. Mino, H. Shinto, S. Sakai, and H. Matsuyama, Effect of internal mass in the lattice Boltzmann simulation of moving solid bodies by the smoothed-profile method, *Phys. Rev. E* **95**, 043309 (2017).
- [24] T. Inamuro, R. Tomita, and F. Ogino, Lattice Boltzmann simulations of drop deformation and breakup in shear flows, *Int. J. Mod. Phys. B* **17**, 21 (2003).
- [25] M. R. Swift, W. R. Osborn, and J. M. Yeomans, Lattice Boltzmann Simulation of Nonideal Fluids, *Phys. Rev. Lett.* **75**, 830 (1995).
- [26] M. R. Swift, E. Orlandini, W. R. Osborn, and J. M. Yeomans, Lattice Boltzmann simulations of liquid-gas and binary fluid systems, *Phys. Rev. E* **54**, 5041 (1996).
- [27] A. J. Briant, A. J. Wagner, and J. M. Yeomans, Lattice Boltzmann simulations of contact line motion. I. Liquid-gas systems, *Phys. Rev. E* **69**, 031602 (2004).
- [28] J. W. Cahn, Critical point wetting, *J. Chem. Phys.* **66**, 3667 (1977).
- [29] D. Iwahara, H. Shinto, M. Miyahara, and K. Higashitani, Liquid drops on homogeneous and chemically heterogeneous surfaces: A two-dimensional lattice Boltzmann study, *Langmuir* **19**, 9086 (2003).
- [30] Y. Nakayama and R. Yamamoto, Simulation method to resolve hydrodynamic interactions in colloidal dispersions, *Phys. Rev. E* **71**, 036707 (2005).
- [31] T. Krüger, H. Kusumaatmaja, A. Kuzmin, O. Shardt, G. Silva, and E. M. Viggen, *The Lattice Boltzmann Method* (Springer International Publishing, Cham, Switzerland, 2017).
- [32] H. Tanaka and T. Araki, Simulation Method of Colloidal Suspensions with Hydrodynamic Interactions: Fluid Particle Dynamics, *Phys. Rev. Lett.* **85**, 1338 (2000).
- [33] T. Inamuro, N. Konishi, and F. Ogino, A Galilean invariant model of the lattice Boltzmann method for multiphase fluid flows using free-energy approach, *Comput. Phys. Commun.* **129**, 32 (2000).
- [34] C. M. Pooley and K. Furtado, Eliminating spurious velocities in the free-energy lattice Boltzmann method, *Phys. Rev. E* **77**, 046702 (2008).
- [35] C. Allain and M. Cloitre, Interaction between particles trapped at fluid interfaces: I. Exact and asymptotic solutions for the force between two horizontal cylinders, *J. Colloid Interface Sci.* **157**, 261 (1993).
- [36] H. Shinto, D. Komiyama, and K. Higashitani, Lattice Boltzmann study of capillary forces between cylindrical particles, *Adv. Powder Technol.* **18**, 643 (2007).
- [37] D. Jacqmin, Calculation of two-phase Navier-Stokes flows using phase-field modeling, *J. Comput. Phys.* **155**, 96 (1999).
- [38] N. D. Denkov, O. D. Velev, P. A. Kralchevski, I. B. Ivanov, H. Yoshimura, and K. Nagayama, Mechanism of formation of two-dimensional crystals from latex particles on substrates, *Langmuir* **8**, 3183 (1992).
- [39] A. Mazloomi M, S. S. Chikatamarla, and I. V. Karlin, Entropic Lattice Boltzmann Method for Multiphase Flows, *Phys. Rev. Lett.* **114**, 174502 (2015).
- [40] T. Inamuro, T. Yokoyama, K. Tanaka, and M. Taniguchi, An improved lattice Boltzmann method for incompressible two-phase flows with large density differences, *Comput. Fluids* **137**, 55 (2016).
- [41] M. Abramowitz and I. A. Stegun, *Handbook of Mathematical Functions with Formulas, Graphs, and Mathematical Tables* (Dover Publications, New York, 1972).